GeoScienceWorld
Lithosphere
Volume 2022, Article ID 8100224, 27 pages
https://doi.org/10.2113/2022/8100224

Lithosphere

Research Article

High-Detail Fault Segmentation: Deep Insight into the Anatomy of the 1983 Borah Peak Earthquake Rupture Zone (M_w 6.9, Idaho, USA)

Simone Bello,[1,2] **Carlo Andrenacci**,[1] **Daniele Cirillo**,[1,2] **Chelsea P. Scott**,[3] **Francesco Brozzetti**,[1,2] **J Ramon Arrowsmith**,[3] **and Giusy Lavecchia**[1,2]

[1]*DiSPuTer, University G. d'Annunzio, via dei Vestini 31, Chieti 66100, Italy*
[2]*CRUST-Centro inteRUniversitario per l'analisi Sismotettonica Tridimensionale, Italy*
[3]*School of Earth and Space Exploration, Arizona State University, 781 Terrace Mall, Tempe, AZ 85287, USA*

Correspondence should be addressed to Simone Bello; simone.bello@unich.it

Received 31 August 2021; Accepted 7 December 2021; Published 14 March 2022

Academic Editor: Songjian Ao

Following observations made in a survey campaign along the Lost River Fault (Idaho, USA) in 2019, we integrate both original and previously published data to obtain a detailed segmentation of the fault sections that failed in the 1983 Borah Peak earthquake (M_w 6.9). The earthquake ruptured the topographic surface with an oblique-normal faulting mechanism, activating two SW-dipping fault segments (Thousand Springs and Warm Springs) and a branching SSW-dipping fault (Arentson Gulch Fault) and producing coseismic surface ruptures with up to 3 m of vertical separation. We augment the 1983 earthquake description by interpreting high-resolution topography and fault mapping. We use quality vertical separation data, rupture zone width measurements, and fault slip data to analyze major and minor structural-geometric complexities, highlighting a partition of the deformation and a fault segmentation into four detail levels (i.e., segments, sections, subsections, and sectors). Our work provides new details of the 1983 Borah Peak earthquake, constraints for paleoseismic and seismotectonic studies, and a methodological approach applicable in other areas of the world. Our fault-slip data show variations along fault-strike that we interpret as kinematic partitioning. In 1983, the main southern segment had a large rupture zone width, while the northern segment localized the deformation. The distributed ruptures accommodate a large portion of the rupture length (~19.5 km versus 31 km for the main rupture) and displacement (~66%). 83% of the surface faulting and 80% of the displacement are located at the hanging wall of the main rupture. There is a strong correlation between vertical separation, rupture zone width, rupture position (footwall or hanging wall), and fault geometry. We highlight the control of the obliquity and kinematic partitioning in the surface expression of the earthquake propagation. We interpret the coseismic (i.e., 1983) and long-term (i.e., Quaternary) behavior, showing that the two activated segments had similar cumulated behaviors in distributing the deformation between synthetic and antithetic ruptures, despite the different geometries. Our results have implications for fault rupture behavior with application to rupture hazard.

1. Introduction

Research on surface faulting and deformation forms the foundation of seismic hazard research and thus requires that faults are correctly segmented. Researchers assess maximum likely earthquake magnitudes and rupture patterns from fault geometry, segmentation, hierarchy, and interaction and results are used in for urban planning [1, 2].

The 1983 Borah Peak earthquake (1983Eq) occurred along the Lost River Fault in the northernmost portion of the Basin and Range Province, (Figure 1(a); [3]) the same region as the 1959 Hebgen Lake (M_w 7.2; e.g., [4]) and Stanley earthquakes (2019, M_w 6.5; [5]). The oblique-normal 1983Eq ruptured ~35 km of the ~130 km-long Lost River Fault (LRF) in south-eastern Idaho (Figure 1(a)) and activated the ~SW-dipping Thousand Springs Segment and

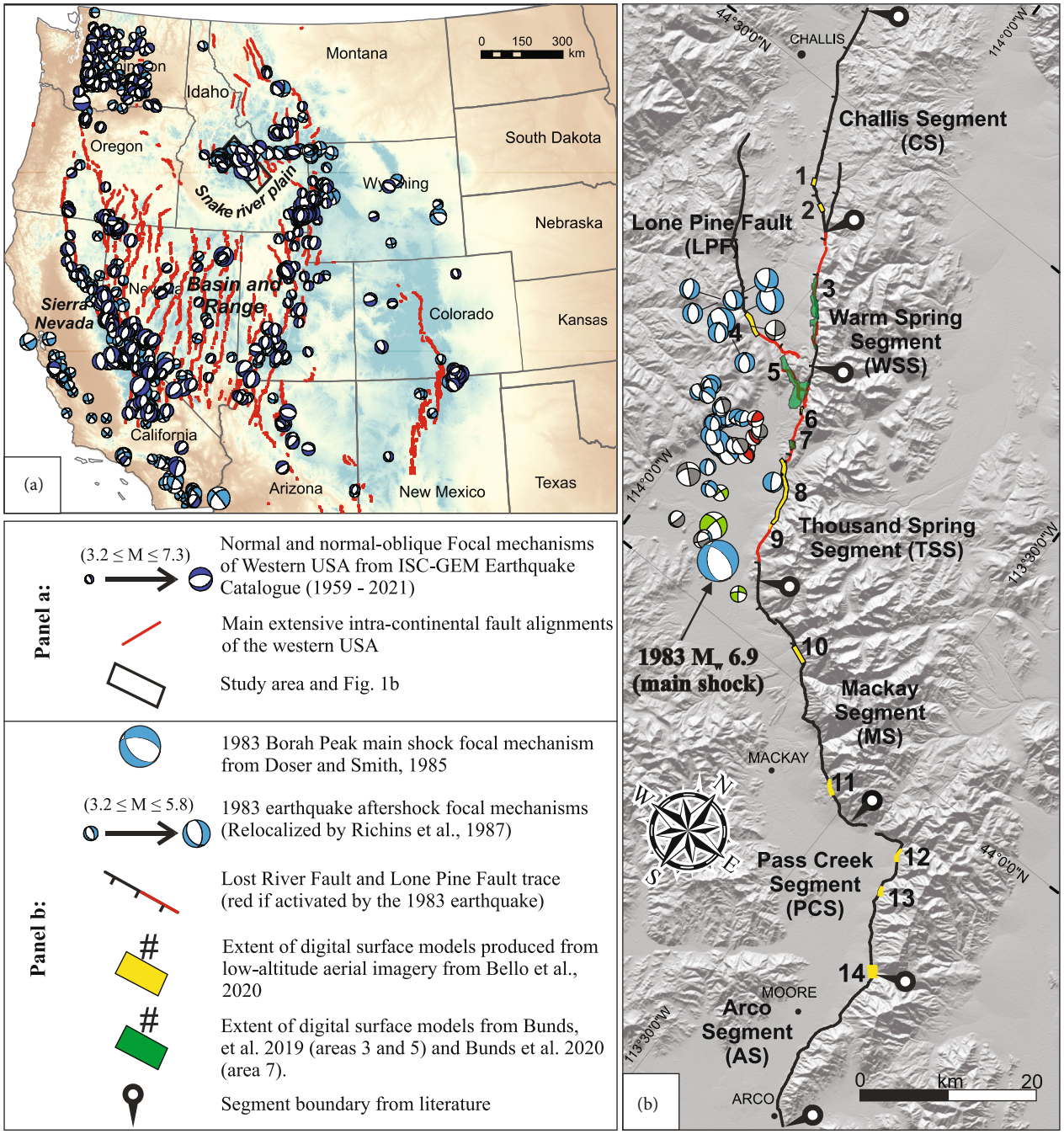

FIGURE 1: Regional location map and study area. (a) Location of the Lost River Fault (LRF, eastern-central Idaho) in the northern Basin and Range extensional intracontinental tectonic province of the western USA. The major normal faults are from U.S. Geological Survey [16]. The Western USA earthquake focal mechanisms ($3.0 \leq M_w \leq 6.9$) from 18 August 1959 to 31 March 2021 are from ISC-GEM Earthquake Catalogue, divided into dark-blue (normal) and light-blue (oblique) [51–53]. (b) LRF [54] divided into its six segments (Challis, Warm Springs, Thousand Springs, Mackay, Pass Creek, and Arco). Black lines show the LRF with ticks on downthrown side. Red lines show the portion of the LRF activated during the 1983 Borah Peak earthquake. Numbered polygons show areas mapped with high-resolution topography (yellow = Bello et al., [55]; green = Bunds et al., [49, 50]). Numbering as in Bello et al., [55]. The background is 30 m shaded-DEM. The 1983 Borah Peak mainshock focal mechanism is from Doser and Smith [12], while aftershocks focal mechanisms are from Richins et al. [10]. Aftershock focal mechanisms colors indicate the following different senses of motion: blue: normal; light-green: strike-slip; dark green: oblique normal; red: reverse.

Warm Springs Segment and~5 km along the ~SSW-dipping Arentson Gulch Fault (Figure 1(b)), producing surface faulting with a coseismic throw of ~3 m (e.g., [6–8]) and several million dollars in damage to infrastructure and buildings [9].

Following the 1983Eq, researchers examined the seismic activity with temporary seismic networks [10, 11]. The aftershocks mainly concentrated north of the mainshock along the southwestern portion (~parallel to the surface ruptures)

of the LRF, covering an area of 75 × 10 km with a NW-SE trend [10]. The largest aftershock (M_l 5.8) occurred about 6 hours after the mainshock. Seismological cross-sections show widespread seismicity along a steeply NE-dipping fault in the northwest [11] and a moderate (~45-50°) SW-dipping fault along the central and southern portions of the fault [10]. This plane of seismicity corresponds with the seismogenic source [12–15]. The USGS Earthquake Catalog [16] for the year following the mainshock highlights two clusters: the 21 March-13 April 1984 cluster with M 3.0-4.2 events was located ~50 km NW of the northern surface rupture termination, and the 22 August-23 September 1984 occurred in the central portion of the Challis segment and the largest event was M_w 5.1. The largest event in the 20 following years had M_l 5.0 [17].

After almost forty years, the coseismic and likely post-seismic surface ruptures produced by the 1983Eq are well preserved, as shown in some representative pictures in Figure 2. Only about fifteen earthquakes produced significant extensional surface ruptures in the last century. These are the 1915 Pleasant Valley (M_w 7.2, USA, e.g., [18]), the 1933 Diexi (M 7.5, China, e.g., [19]), the 1954 Rainbow Mountain-Fairview Peak-Dixie Valley (M_w 7.3, USA, e.g., [20]), the 1959 Hebgen Lake (M_w 7.2, USA, e.g., [4]), the 1980 Mammoth Lake (M_w 6.2, USA, e.g., [21]), the 1980 Irpinia (M_w 6.9, Italy, e.g., [22]), the 1981 Corinth (M_s 6.7, Greece, e.g., [23]), the 1983 Borah Peak (M_w 6.9, USA, e.g., [6]), the 1987 Edgecumbe (M_w 6.2, New Zealand, e.g., [24]), the 1999 Düzce Earthquake (M_w 7.1, Turkey, e.g., [25]), the 2008 Yutian (M_w 7.1, China, e.g., [26]), the 2009 L'Aquila (M_w 6.3, Italy, e.g., [27]), the 2010 El Mayor–Cucapah (M_w 7.2, Mexico, e.g., [28]), the 2016 Parina (M_w 6.1, Peru, e.g., [29]), and the central Italy 2016-2017 (M_w 6.3, Italy, e.g., [30]).

The concept of fault segmentation has been widely applied by researchers who study fault geometry and paleoseismicity of seismogenic faults in the Basin and Range province of the U.S.A (e.g., [2, 31–35]), in the extensional seismotectonic province (*sensu* [36]) of the Italian Apennines (e.g., [22, 30, 37–41]) and among many other places globally. Tectonic structure segmentation depends on the structure shape and interaction with neighboring segments at scales of several to hundreds of kilometers. Although fault segmentation used for seismic hazard analyzes is often based of observations over kilometer scales, many assumptions depend on experimental modeling (centimeter to meter scale, e.g., [42, 43]). Based on geometrical-structural segmentation, researchers divided the LRF into six segments with 18 to 30 km length. From north to south, these segments are Challis (CS), Warm Springs (WSS), Thousand Springs (TSS), Mackay (MS), Pass Creek (PCS), and Arco (AS) [6, 44–48]. For our geometrical segmentation, we incorporate a large and detailed surface deformation from the 1983Eq, which was not done in these previous studies. We consider it essential to exploit the obtainable information before they are obliterated by surface processes.

The increasing availability of high-resolution topography facilitates measuring and analyzing rupture behavior and surface slip distribution at the meter to decameter scale along active faults [7, 8, 49, 50]. We use these observations to better define the fault segmentation given Quaternary and 1983 vertical separation (VS) distributions, rupture zone width (RZW) measurements, geometric-structural complexities, and fault-slip (i.e., slickensides and slickenlines) data. These observations support dividing the Warm Springs and Thousand Springs Segments into lower-order structures, with important implications for the slip distribution and therefore seismic hazard.

In this paper, we identify geometric discontinuities and irregularities along the LRF and specifically for the 1983Eq rupture. We concentrate on the 1983Eq area and constrain four orders of fault segmentation (i.e., segments, sections, subsections, and sectors). We use several datasets including along-strike VS due to both the long-term and 1983 coseismic displacement, RZWs, geometric and structural complexities (e.g., bends, gaps, stepovers) and fault-slip data for kinematic partitioning of the fault.

2. Methods and Data Analysis

Our results are based on a multiscale and multidisciplinary methodology based on structural geology, geomorphology, morpho-tectonics, and geodesy. Recent improvements in small Unmanned Aerial Vehicles (UAV) technology and Structure-from-Motion (SfM) processing techniques (e.g., [56–60]) enable geologists to produce maps of topography and color orthophotos of landscapes at submeter scale resolution. Bello et al. [8, 55] used these approaches to produce high-resolution georeferenced topography and color orthophotos along 21 km of the LRF (Figure 1(b)) at a resolution of 5-30 cm based on aerial imagery collected in April 2019 (areas in yellow in Figure 1(b)). They augmented these data with additional high-resolution georeferenced topography datasets collected in 2015-2016 by Bunds et al. [49, 50] for use in DuRoss et al. [7]. Together, these datasets cover 37 km of the LRF in areas that ruptured in 1983 as well as those that ruptured in Quaternary earthquakes but not in the 1983Eq.

Bello et al. [8] used these three high-resolution datasets to map fault traces along the LRF at a 1:400 scale and recorded if each fault trace was the principal 1983 coseismic rupture (P-CoR), a distributed 1983 coseismic rupture (D-CoR), or an older Quaternary fault scarp (Qfs). The mapped fault traces were used to systematically measure the RZW along the hanging wall (HW) and footwall (FW) of the P-CoR. They made 2053 VS measurements for the 1983 Borah Peak earthquake. Both Bello et al. [8] and DuRoss et al. [7] defined VS as the vertical distance at the fault between best-fit lines projected along the HW and FW ground surfaces, assuming that the surface was continuous before their displacement. To make the VS measurements, Bello et al. [8] took approximately fault perpendicular transects spaced 25 m apart. For each mapped fault, they manually identified the fault location as well as the HW and FW by viewing each transect in section view. They recorded if the VS measurement was a CoR or Qfs and assigned a quality parameter. The VS quantitative error was based on the scatter in the best-fit HW and FW lines and an assumption that the error in fault position is 25% of the VS. The CoRs and Qfs had an average error of 5 cm and 25 cm, respectively, and larger VS had higher uncertainties.

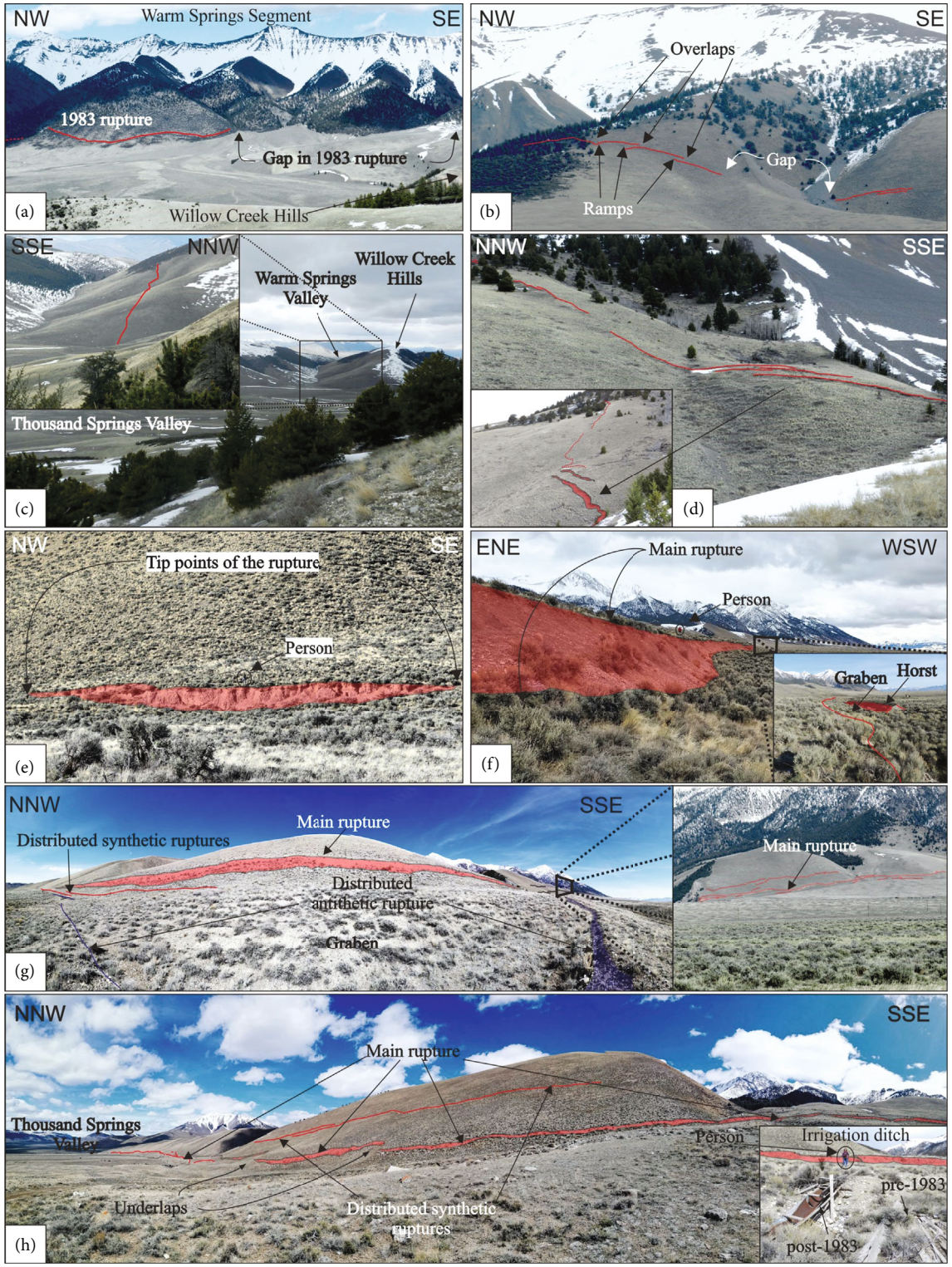

FIGURE 2: 1983 coseismic surface ruptures (CoRs) in representative outcrops in the study area. (a) Panoramic view of the CoRs and the 1983 rupture gap along the Warm Springs Segment. (b) CoRs and a small gap in 1983 rupture in the Dickey Peak area. (c) CoRs along the Arentson Gulch Fault from Dickey Peak. (d) CoRs along the slope of Dickey Peak. (e) 1983 fault scarp ~300 m north of Double Spring Pass road. (f) 1983 fault scarp at Double Spring Pass. (g), (h) CoRs along the Thousand Springs Segment (red and blue lines highlight synthetic and antithetic CoRs, respectively). (h) P-CoRs (principal) and D-CoRs (distributed) outcropping along the central-southern Thousand Springs Segment. The small inset shows the remains of a faulted irrigation ditch restored after the 1983 earthquake close to Birch Springs.

To validate the VS measurements, one hundred of the ruptures were measured by two geologists, and 90 of the measurements by both geologists were within error of each other, indicating minimal operational bias. For a further check on the data validity, they compared 125 VS measurements to 53 measurements from Crone et al. [6] and 72 in DuRoss et al. [7] and showed a good correlation between the three sets of measurements.

In this paper, we use uninterpreted data from Bello et al. [8], unpublished data, and other datasets to research fault segmentation at the subkilometer scale along the fault activated in the 1983Eq, as shown in Figure S1. In particular, we used (1) P-CoRs, D-CoRs, and Qfs, (2) VS measurements, and (3) RZW. We integrate these data with new fault orientation and slip vector slickenline data to research kinematic partitioning.

2.1. Rupture Zone Width along Fault-Strike. RZW measures the rupture-to-rupture distance between the two most distant CoRs located perpendicular to the main fault and indicates fault's tendency to distribute deformation over a wide zone or on a single rupture (i.e., the P-CoR). We used the RZW measurements from Bello et al. [8], which were divided into the footwall (FW-RZW) and hanging wall (HW-RZW). In other words, the RZW measures the fault-perpendicular distance between the principal rupture and the most distant rupture at the FW and HW along a straight line (i.e., a topographic profile). To obtain a representative position for the RZW, we use the "Near Analysis" tool in ArcMap ArcGIS® to project each RZW to a central point along the nearest topographic profile. To integrate the RZW dataset into the 1983Eq rupture segmentation model, we identify areas with significant variations in RZW (Figures 3 and 4). Along the 1983Eq fault segments, RZW shows a strong variability (see Figure 3). While along the Warm Springs Segment, deformation is concentrated almost exclusively on the P-CoR trace, along the Arentson Gulch Fault and Thousand Springs Segment, RZWs varies on a several hundred meters scale. The conceptual 3D model in Figure 4(e) shows the RZW divided into HW and FW portions and their prosecution at shallow depth.

As shown in the frequency distribution histogram in Figure 4(f), the 1983 surface deformation was concentrated on the P-CoR (i.e., RZW = 0). Most of the ruptures along the HW are within 220 m of the P-CoR, with peaks located between 10 and 70 m. Along the FW, the deformation is almost entirely contained within 120 m of the P-CoR. Note that there is FW-RZW along the Warm Springs Segment and Thousand Spring Segment, but there is only HW-RZW for the Arentson Gulch Fault. As shown in Figure 4, HW, FW, and Tot-RZW have two well-defined peaks of ~300 m in the central portion of Thousand Springs Segment. A local ~200 m peak is located ~3 km south of Double Springs Pass road, where the fault bifurcates and sharply changes strike (see Figure 3(b)). High FW-RZW correlate with changes in fault strike and stepovers between en-échelon P-CoRs. HW-RZW almost always exceeds FW-RZW, except along certain geometric and structural complexities described in the section "Geometric and Structural Complexities."

2.2. Vertical Separation along Fault-Strike. The 1983Eq produced ~35 km of surface ruptures along the Thousand Springs Segment and Warm Springs Segment and ~5 km along the Arentson Gulch Fault which is a branch fault at Willow Creek Hills. There are two gaps in 1983 ruptures that are ~2.7 km and ~4.5 km long located along the Warm Springs Segment. Crone et al. [6] measured the vertical and horizontal displacement components using tape, compass, and level in 107 locations along CoRs and 35 scarp heights (along Qfs) over the entire rupture. DuRoss et al. [7] acquired 196 VS measurements of CoRs and 56 VS measurements of Qfs along the Warm Springs Segment and the Arentson Gulch Fault. Bello et al. [8] acquired 2050 VS measurements along the Warm Springs Segment, Thousand Springs Segment, and Arentson Gulch Fault (1431 VSs of CoRs and 662 of Qfs). They distinguished CoRs from Qfs in the DEMs, orthomosaics, and 3D models. To measure VS, they picked four points within a few meters of the CoRs and tens of meters of the Qfs. Here, we integrate the VS data from these three studies organizing them in shapefiles and managed in ESRI ArcMap ArcGIS® 10.8, with the assumption that all the coseismic ruptures have a common primary tectonic origin, as also supported by DuRoss et al. ([7]; their Figure 12(b)). Bello et al. [8] assigned a quality parameter called the Measure Quality Ranking (MQR) to all VS measurements. VSs with a MQR 1 and 4 are high and low quality, respectively. The ranking is based on the presence of vegetation, the angle between the linear surface projections at the HW and FW, and the trace position. Here, we use data with rankings of 1 or 2 (high quality) and discard the low-quality data with rankings of 3 and 4. We show the data selected in area 8 in Figure 5. See Figures S2-S4 in the Supplementary Material for comprehensive data selection of areas 3, 4, 5, 6, 7, and 9.

To characterize the surface deformation, we plotted VS along fault-strike. We plotted the VS measurements of P-CoR, D-CoRs, and Qfs from Bello et al. [8] in Figure 6(a) and those along the Arentson Gulch Fault in Figure 6(b), integrating with measurements from Crone et al. [6] to have complete VS profiles along the entire rupture. The coseismic ruptures form a wide deformation zone and have a complex pattern. These ruptures are arranged in principal and distributed, synthetic and antithetic, approximately parallel to each other. Using along-strike profiles of the VS of CoRs and Qfs for the LRF and the Arentson Gulch Fault, we computed envelope curves over 2 and 30 sample intervals. We used the "envelope" function of the Signal Processing Toolbox in MATLAB (http://www.mathworks.com). This function traces the envelopes of the upper and lower peaks of the input signal using spline interpolations over local maxima separated by a given sampling interval. We discuss the results of this analysis in the "Results and Discussions" section.

2.3. Kinematic and Structural Analysis

2.3.1. Geometric and Structural Complexities. The geometric and structural complexities and the morpho-structural features along a normal fault rupture zone have long been the

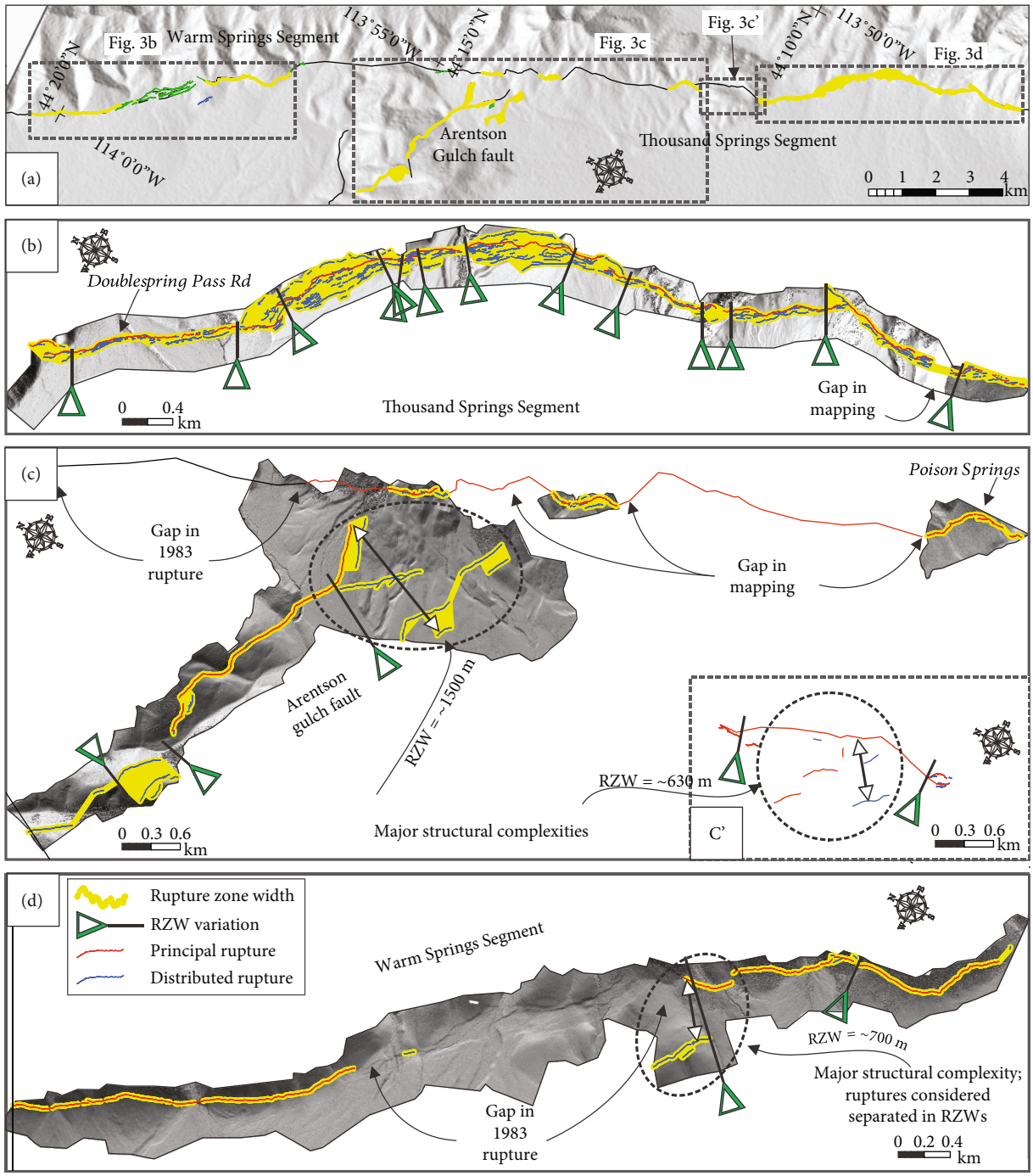

FIGURE 3: (a) RZW along the Thousand Springs Segment, Warm Springs Segment, and Arentson Gulch Fault. Pins highlight sudden changes in RZW. Dashed rectangles are zooms to (b) area 8, (c) area 5, 6, and 7, and (d) area 3 (location map in Figure 1). The mapping in the inset of (c) is from Crone et al. [6].

focus of geological research. We reference the reader to [61–66] for a discussion of the terminology.

The CoRs of the 1983Eq are distributed along the activated segments in geometrically complex patterns (see 3D model of an exemplary area along Thousand Springs Segment in Supplementary Material Figure S5). This deformation is more developed in the central-southern portions of the fault (i.e., Arentson Gulch Fault and Thousand Springs Segment, as discussed above), but geometric and structural complexities of the fault pattern are present along the entire extent of the fault responsible for the 1983Eq.

As a first step in identifying the minor geometric complexities, we used a geo-statistics tool in GIS environment, the Natural Neighbor function of the Spatial Analyst tool of ESRI ArcToolBox, which conducts a moving average in a geospatial reference frame. We used as input the VS measurements. The Natural Neighbor algorithm calculates the

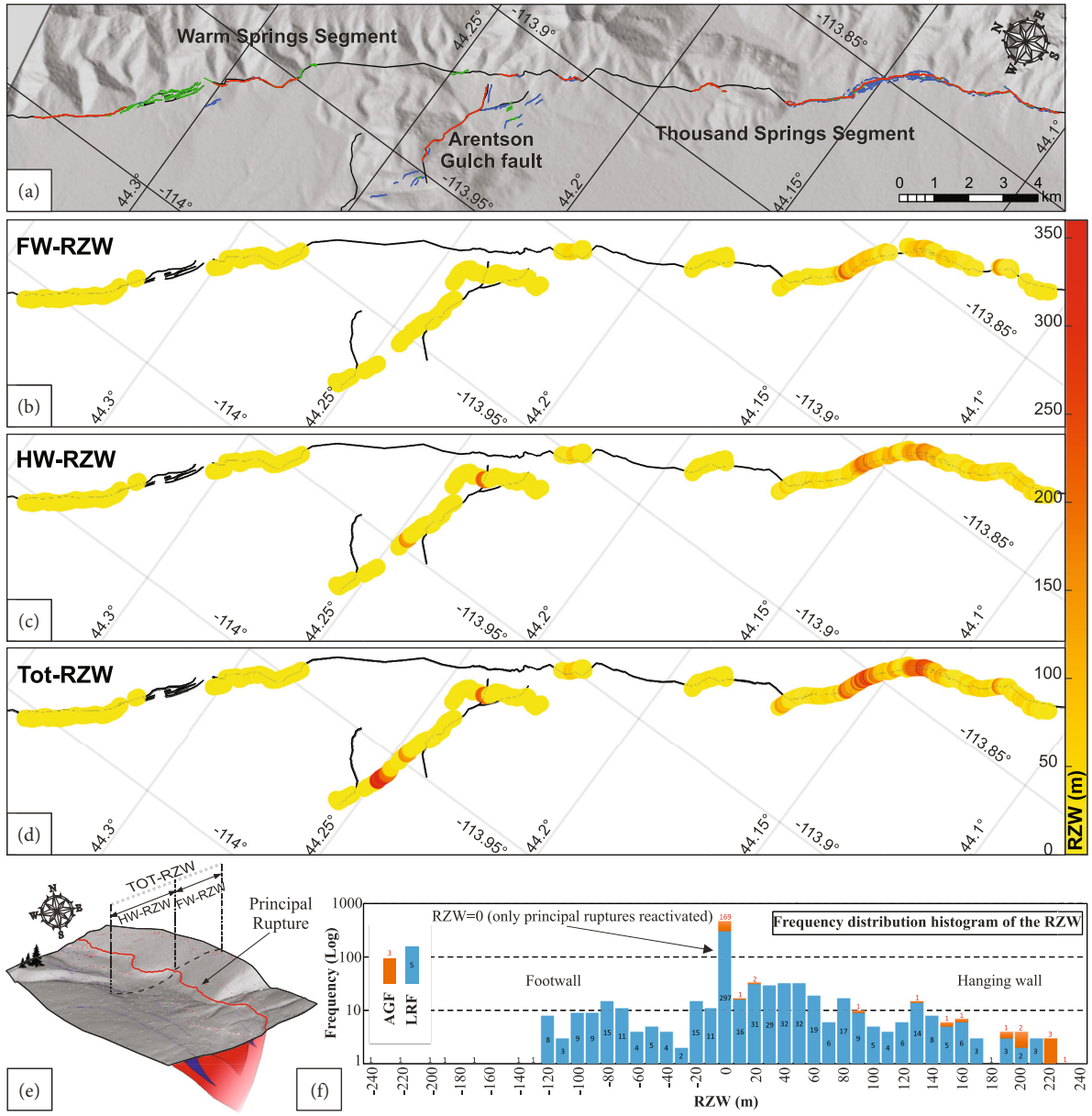

FIGURE 4: RZW along fault-strike. (a) 1983Eq fault trace. Explanation as in Figure 3. (b) FW-RZW (c) HW-RZW, and (d) Tot-RZW. (e) 3D conceptual model of HW, FW, and Tot-RZW. (f) Histogram of the RZW frequency distribution where negative and positive values correspond to the FW-RZW and HW-RZW, respectively.

distance of a point to its nearest neighbors. Each pixel is assigned the average VS value of the neighboring points, obtaining a raster with a 1 m pixel resolution. We cut the raster obtained with a buffer of 20 meters from the P-CoR, with the method of the "extract by mask" tool (ESRI ArcMap). Finally, we overlayed the raster above the hillshaded DEMs [49, 50, 55]. With this approach, we identified areas where the VS variations indicated (1) connecting ruptures and relay ramps, (2) en-échelon patterns, (3) stepovers (underlaps or overlaps), (4) gaps, and (5) isolated faults (e.g., lens-shaped). These results are shown in Figure 7.

We manually mapped all the geometric complexities highlighted along the fault traces published in Bello et al. [8] and integrated them with the geometric-structural complexities that were not directly related to the along-strike VS variation and so not highlighted with the geo-statistical analysis. The integration of this information allowed us to identify the following factors correlated to geometric-structural complexities:

(1) Sudden changes in VS values (ΔVS), divided into three orders: 1st order: $\Delta VS > 130$ cm; 2nd order: 90 cm $< \Delta VS <$ 130 cm;
3rd order = 30 cm $< \Delta VS <$ 80 cm

(2) Gaps among CoRs, divided into three orders: 1st order: gap > 300 m; 2nd order: 100 m < gap < 300 m; 3rd order: gap < 100 m

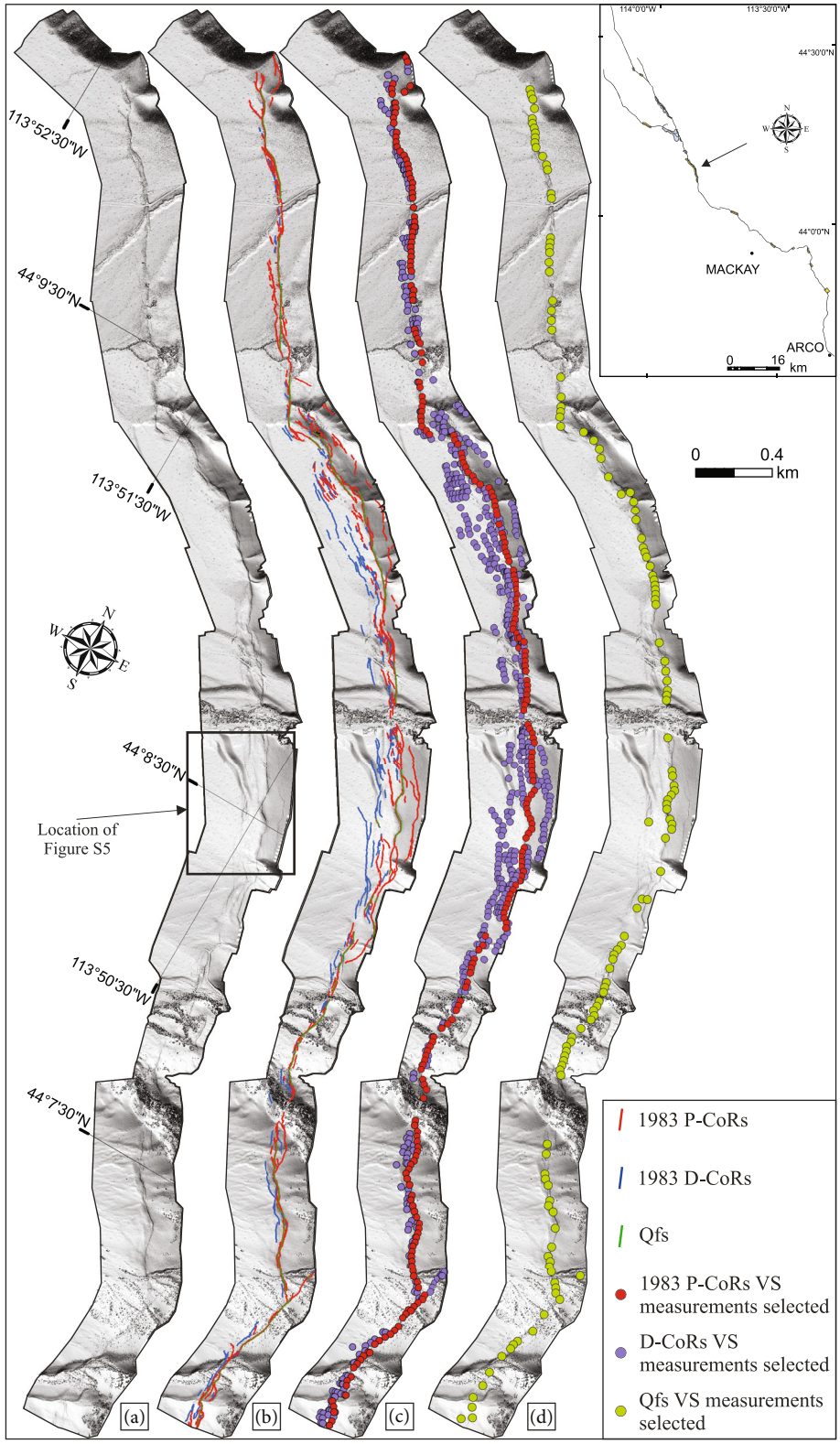

FIGURE 5: (a) High-resolution topography along area 8 at the Thousand Springs Segment [55]. The black rectangle indicates the location of Figure S5. (b) CoRs and Qfs mapped in Bello et al. [8]. (c) High-quality VS of P-and D-CoRs measurements (MQR is 1or 2). (d) High-quality Qfs VS measurements (MQR is 1 or 2).

FIGURE 6: Along fault-strike VS profiles. (a) Qfs and CoRs VS measurements along the Thousand Springs and Warm Springs Segments (from Bello et al. [8]). (b) CoRs VS measurements from Bello et al. [8] and Crone et al. [6] along the Thousand Springs and Warm Springs Segments. (c) Map view of the Thousand Springs and Warm Springs Segments. (d) Qfs and CoRs VS measurements along Arentson Gulch Fault [6–8]. (e) Map view of the Arentson Gulch Fault. Error bars in (a), (b), and (d) correspond to quantitative uncertainty computed in Bello et al. [8] and minimum and maximum values from DuRoss et al. [7] and are omitted for Crone et al. [6] values because they were not reported.

(3) Sudden changes in the RZW (ΔRZW), divided into three orders: 1st order = ΔRZW > 150 m; 2nd order = 100 m < ΔRZW < 150 m; 3rd order = ΔRZW < 100 m

(4) Sharp strike changes (ΔStrike), divided into three orders: 1st order = ΔStrike > 30°; 2nd order = 20° < ΔStrike < 30°; 3rd order = ΔStrike < 20°

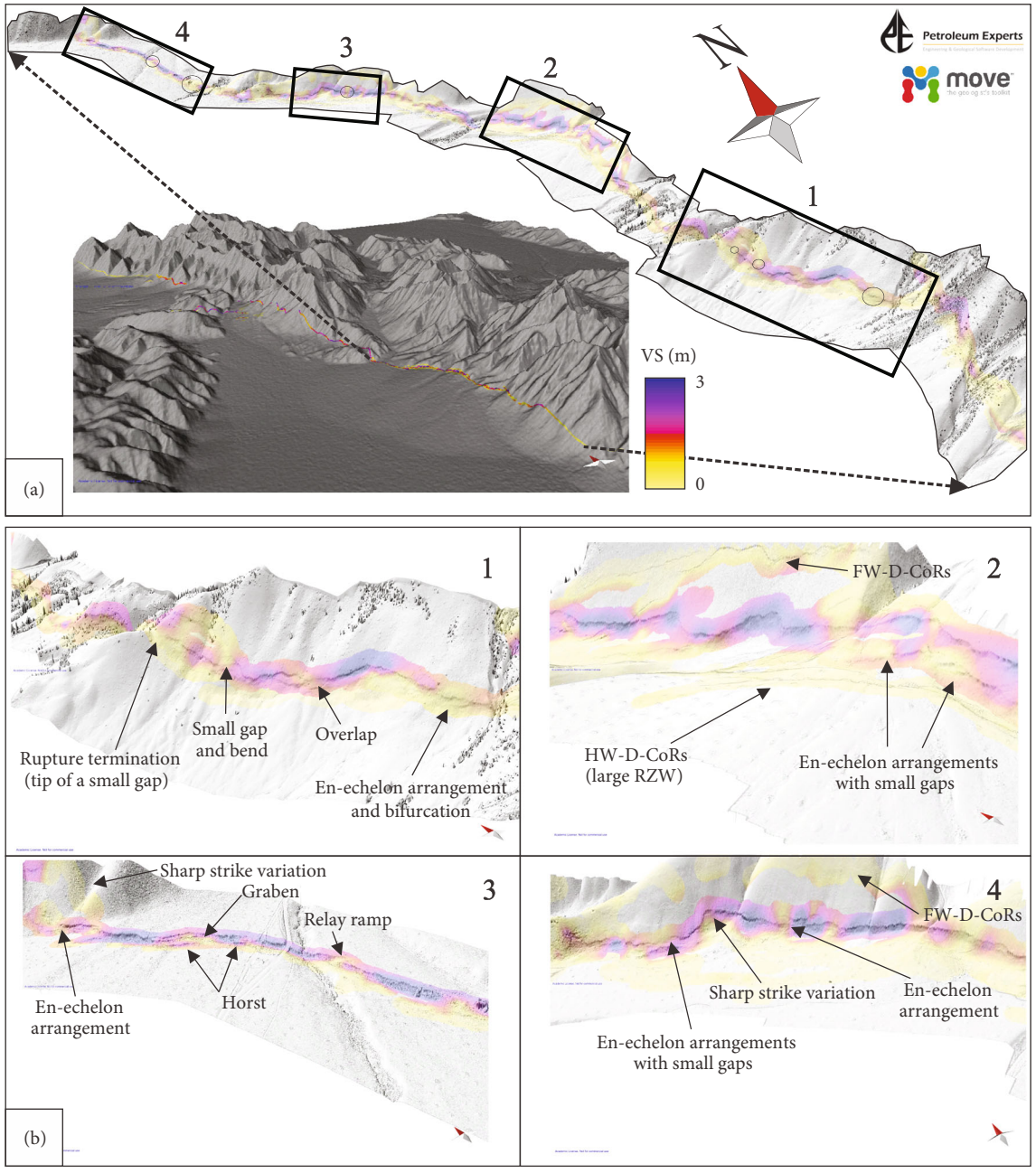

FIGURE 7: Geostatistical analysis used to identify the minor geometric complexities. Input for the statistical interpolation is the VS measurements. (a) High-resolution topography (top) with density contour showing the geostatistical analysis along the Thousand Springs Segment. 3D model (lower left) produced with a 30 m resolution DEM in Move software. (b) Details from area 8 of high-resolution topography in Bello et al. [8] with arrows showing geometric complexities.

(5) The presence of transfer faults and stepover zones (i.e., overlaps, underlaps, and en-échelon arrangements)

These factors are often interrelated, and combinations of them are frequent (e.g., ΔVS and gaps, stepovers, and RZWs, en-echelon arrangements, and RZW). Therefore, we analyzed each separately, and then, we integrated with the other datasets. In particular, characteristics of all orders were used in the segmentation pattern (Section 3.2). We show an example of each feature in Figure 8, where areas have major complexities (MC; Figure 8(b)) or minor complexities (mc; Figure 8(c)). For completeness, we compared the features with the models (block diagrams) from the literature and compiled a panel in the supplementary material (Figure S6).

2.3.2. Slip Vectors from Field Data. In April 2019, we completed a field campaign over the entire LRF to acquire long-term and coseismic fault-slip data (i.e., slickensides and slickenlines). We recorded 286 measurements of fault and bedding orientation and slip vectors on a tablet

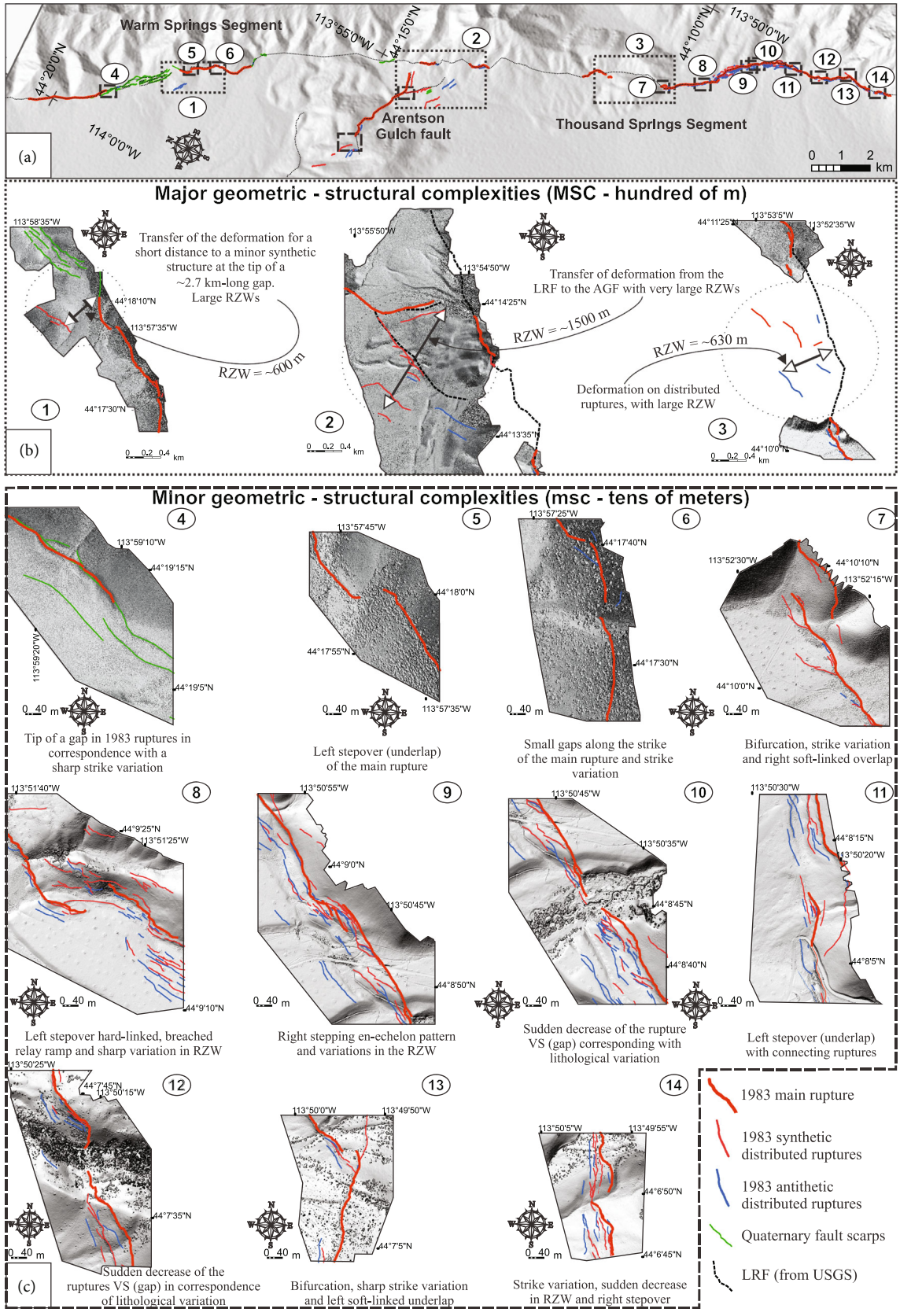

FIGURE 8: Examples of geometric and structural complexities surrounding the 1983Eq. Refer to Figure S6 for a detailed description of complexity types. (a) Location map of the examples in (b) and (c). Dotted and dashed rectangles show major and minor complexities, respectively.

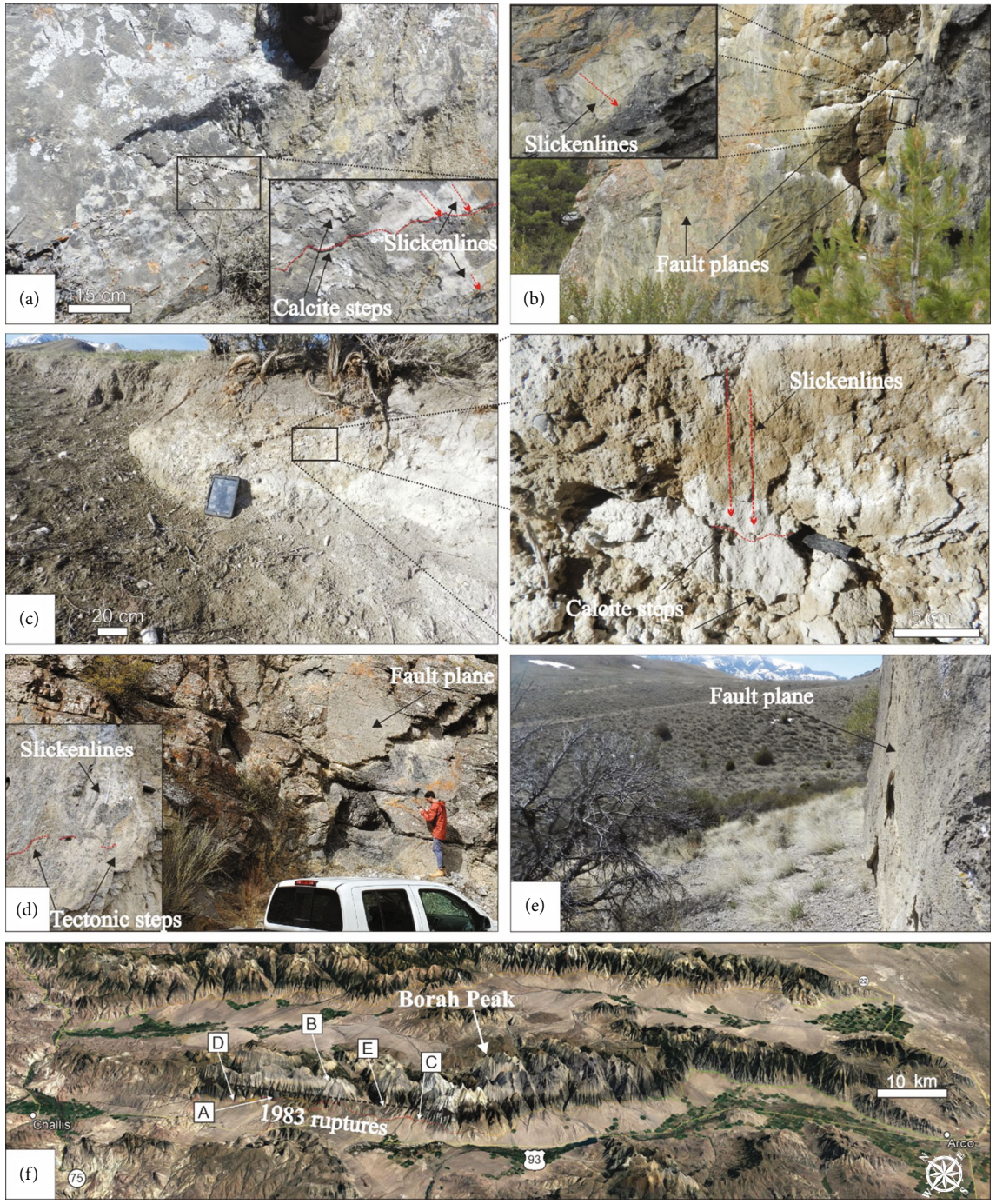

FIGURE 9: (a–e) Representative outcrops along fault segments activated in 1983Eq. (a, b, d, and e) Slickenlines and calcite steps that we used as slip vectors, measured on fault planes, at the bedrock-recent deposits (e.g., fans, alluvium, and colluvium) contact or at the deposits-deposits contact ((c) and its zoom). Photograph locations in (e).

computer using the Petroleum Experts FieldMove software (http://www.petex.com/products/move-suite/digital-field-mapping/). Figure 9 shows representative outcrops of the 1983Eq epicentral area. We also analyze fault net throw (NT) and strike-slip offset (SS) measurements from Crone et al. [6] by digitizing their three plates using ESRI ArcMap ArcGIS® software. They collected the data in the months to years immediately following the 1983Eq. We used ~140 NT and SS of their measurements to calculate the coseismic pitch for the 1983 earthquake.

In Figure 10(a), we represent a normal fault plane that is separated into HW and FW blocks. The throw is DA, and the sinistral strike-slip offset is BC (equal GF). DC (equal to EF) is the Net Slip (NS) along the fault plane. The piercing point is represented by the connection between points E and F, joined in the prerupturing phase. The angle along the fault

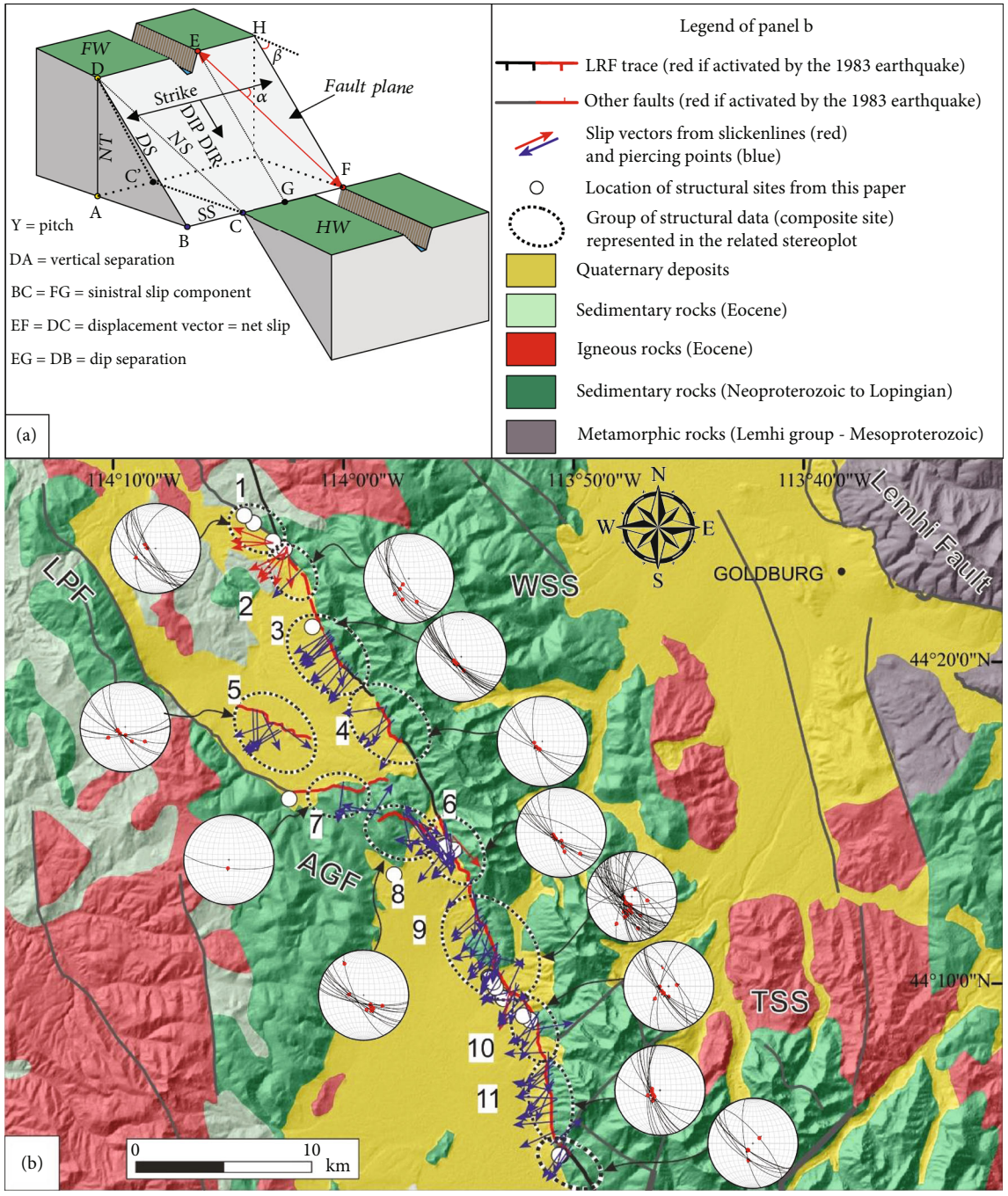

FIGURE 10: (a) Block diagram showing an oblique-normal fault. FW: footwall; HW: hanging wall; NT: Net Throw; DS: Dip Separation; NS: Net Slip; SS: Strike-Slip component; α: pitch-angle; β: dip-angle of the fault plane. (b) Structural–geological map of Warm Springs, Thousand Springs, and Arentson Gulch Faults. Rock types are from the Geologic Map of Idaho, 2012 [54].

plane between EF and the strike line is the pitch (α). DB (equal to EG) is the Dip Separation (DS). The angle β represents the fault plane dip with respect to the horizontal. The strike-slip offset is measured on the BC (or GF) segment for fault planes with $0 < \beta < 89$; for a vertical fault plane ($\beta = 90$), the strike-slip component is given by the AC segment.

Following Xu et al. [67] using the first trigonometric theorem, we establish relationships between SS, NS, NT, DS, α, and β and obtain α, NS, and DS. Although coseismic ruptures in soft deposits often cut the surface with high angles (>70°), we assume that the dip of the fault plane varies between 60° and 90° following Crone et al. [6]. We calculate NS and pitch using β_{min} (60°), β_{max} (90°), and β_{mean} (75°) with results in Supplementary Data 1. We find that pitch varies minimally depending on the chosen β (within ±3°).

Using the nomenclature assigned in Figure 10(a), we obtain:

$$\text{Pitch}(\alpha) = \tan^{-1}\left(\frac{\text{Net Throw}}{\text{Strike Slip} \times \sin\,(\text{Dip Angle})}\right),$$
$$\text{Net Slip} = \frac{\text{Strike Slip}}{\cos\,(\text{Pitch})}. \quad (1)$$

With SS and NT, we calculate DS as:

$$\text{DS} = \sqrt{\text{NS}^2 - \text{SS}^2}. \quad (2)$$

The steps for deriving these parameters are reported in full detail in Supplementary Text 1.

We grouped the results calculated with the above into 12 survey sites. In Figure 10(b), we plot the slip vectors in lower hemisphere stereographic projections on the structural-geological map, with the rock types to show the geologic contacts between the HW and FW of the faults in the 1983Eq [54]. We analyzed the fault-slip data with pseudo-focal mechanisms for each survey site with FaultKin7 software from Allmendinger et al. [68] with results shown in Table 1 and Supplementary Figure S7. The reported rake is in Aki-Richards format. We computed the *T*-axis trend and plunge by applying the dihedron angle method to the fault populations [69]. We provide a georeferenced dataset of the structural observations, slip magnitude, and direction measurements in Supplementary Data 1. The shapefile folder of Supplementary Data 1 contains a table describing the attribute fields.

3. Results and Discussion

3.1. Geometric and Statistical Properties of the 1983Eq Surface Deformation. We discuss observations from the CoRs and Qfs traces [8] that show a characteristic behavior of the segments activated during the 1983Eq. The P-CoRs from the 1983Eq have an average N140 strike with some ruptures striking between N100 and N160 (see Figure S8a and S9). However, while the synthetic D-CoRs in the HW have a strike similar to the P-CoRs (see the best fit lines in Figure S8a), the D-CoRs in the FW have an average N120 strike, which decreases as the length of the CoR increases. There is a similar trend for the antithetic D-CoRs: they strike in the HW and FW ~N315 and ~N290, respectively. This suggests that the HW and FW location has a direct control on the deformation.

For the entire 1983Eq, ~69% ($n = 353$) of CoRs occur on the HW, 15% on the FW ($n = 72$), and 16% represent the P-CoR ($n = 84$). Normalizing CoRs based on their length shows that 47.2% of the D-CoRs are located at HW, 9.4% at FW, and 43.4% are the P-CoR (see Supplementary Material, Figure S9).

Of all the traces mapped, 48% and 39% are synthetic and antithetic CoRs, respectively, and 9% and 4% are synthetic and antithetic Qfs. Normalizing by length shows that 73% of the CoRs and 76% of the Qfs are synthetic. Although this observation is not representative of the whole fault, this suggests an even distribution of synthetic and antithetic structures along the Warm Springs and Thousand Springs Segments over time (see Supplementary Material Figure S9).

90% of the CoRs are less than 150 m in length, and the maximum length is over 2000 m (Figure S9). Many CoRs break the topographic surface for a few tens or hundreds of meters, close and transfer deformation to nearby CoRs (see Figures 2(e), 2(h), 6(b), and S5). Longer CoRs have greater VS (see Figure S8b and S9). CoRs with higher VS strike N100-N180, and CoRs with peaking VS of ~3 m strike N160 (Figure S8c). The D-CoRs accommodate ~66% of the surface deformation [8] and represent 19.5 km of the total 31 km rupture length.

Following Boncio et al. [70] approach for thrust faulting, we analyzed RZW measurements for relative frequency and cumulative distribution (Figure 11) for the HW and FW with probability density functions. The HW data (Figures 11(a) and 11(b)) show a high frequency of 0-2 m, indicating that most of the 1983Eq-related surface deformation was concentrated on or close to the P-CoR (Figure 11(b)). 64% of the fault has a 0 m RZW. Most of the rest of the data have 4-72 m RZW. Along the HW, we used the Gamma cumulative distribution and probability density function to divide the statistical distribution into discrete frequency intervals of 35%, 50%, 75%, and 90%. A probability of 35% (HW35) corresponds to a 1.5 distance from the P-CoR. A 50% probability has a 5 m RZW. 75% (HW75) and 90% (HW90) probabilities have distances from the P-CoRs of 26.5 m and 72 m, respectively.

The FW data show a similar trend to the HW (Figures 11(c) and 11(d)), with a 0-2 m frequency of the P-CoR (Figure 11(d)). The cumulative frequency is 0.82 m, confirming that the deformation is concentrated along the P-CoR and only in some areas D-CoRs occur at high distances on the FW (Figure 11(c)). The FW histogram shows very low frequencies for RZWs of 4-116 m, tending to 0 for greater distances. We calculated the RZW values related to specific probability percentages using the Gamma Cumulative Distribution Function curve. In correspondence with a probability of 35% (FW35) and 50% (FW50) the values of the distance from the P-CoR are low (0.3 m and 1 m, respectively). 75% (FW75) and 90% (FW90) probabilities have distances from the P-CoR of 7 m and 35 m, respectively.

In Figure 11(e), we report the different RZW values for different selected probabilities (90, 75, 50, and 35%) relating to HW (HW-RZW), FW (FW-RZW), and total RZW (Tot-RZW). We calculated the ratios between FW-RZW and HW-RZW. These ratios vary from a minimum of 1 : 2 for the probability density of 90% up to a maximum of 1 : 5 for the probability density of 50% and 35% which determines an average ratio of ~1 : 4. We find this ratio consistent with the deformation patterns in active normal faults environments (e.g., [71]), although it is not uniformly distributed across the ruptured fault.

To verify the above relationships, we compared Tot-RZW, Tot-VS for the CoRs, and Tot-VS for the Qfs in areas with at least two of the three parameters. Tot-RZW is the sum of RZW along the HW and FW, and the Tot-VS is the sum of the absolute values of the respective VS measurements (i.e., Net VS). Figure S10 does not show a true correlation between these parameters. In particular, total

Table 1: Pseudo-focal mechanisms. Site number corresponds to the data group in Figure 10. Site numbers with asterisks span the 1983 rupture. PFS: pseudo-focal mechanisms computed from structural data. Data *N*: number of fault planes and slip vector measurements. F/S *n*: number of measurements used in the pseudo-focal mechanism calculation. Seg.: LRF segments (CHS: Challis Segment; WSS: Warm Spring Segment; WSS-s: synthetic splay of the Warm Spring Segment; TSS: Thousand Springs Segment; LPF: Lone Pine Fault; MS: Mackay Segment; PCS: Pass Creek Segment; AS: Arco Segment). Seg. dip dir.: the segment's dip direction. Rake is in Aki-Richards's format. *T*-axes (trend/plunge) were computed with the dihedron angle method [69]. *Average attitude calculated only from the main synthetic faults. pseudo-focal mechanisms and parameters are reported in Figure S7.

Site n.	PFM	Data n.	F/S n.	Seg.	Seg. dip dir. (deg.)	Mean plane strike* (deg.)	Mean plane dip* (deg.)	Mean slip vector trend* (deg.)	Mean slip vector plunge* (deg.)	Rake (A-R)	T-trend (deg.)	T-plunge (deg.)
1		13	8	CHS	243	159.5	64.5	263.6	63.8	-96.2	254.1	19.2
2*		14	12	WSS	238	142.3	63.8	208.7	61.7	-79	224.2	18.1
3*		30	30	WSS	238	134.9	75.0	219.6	74.9	-88.6	223.8	30
4*		10	10	WSS	238	135.8	74.9	224.6	74.9	-89.7	225.6	29.9
5*		16	16	WSS-s	205	115.9	73.6	180.4	72.0	-82.3	199.8	28.2
6*		18	16	TSS	246	133.2	74.3	186.7	70.7	-78.7	214.1	28.4
7*		2	2	LPF	021	097.0	75.0	187.0	75.0	-90	187.0	30.0
8*		22	22	TSS	246	113.6	76.1	153.0	68.8	-73.7	190.5	29.3
9*		169	98	TSS	246	159.0	74.3	243.4	74.2	-88.5	247.8	29.3
10*		22	22	TSS	246	151.2	66.5	239.9	66.5	-89.5	240.8	21.5
11*		22	22	TSS	246	159.0	74.3	243.4	74.2	-88.5	247.8	29.3

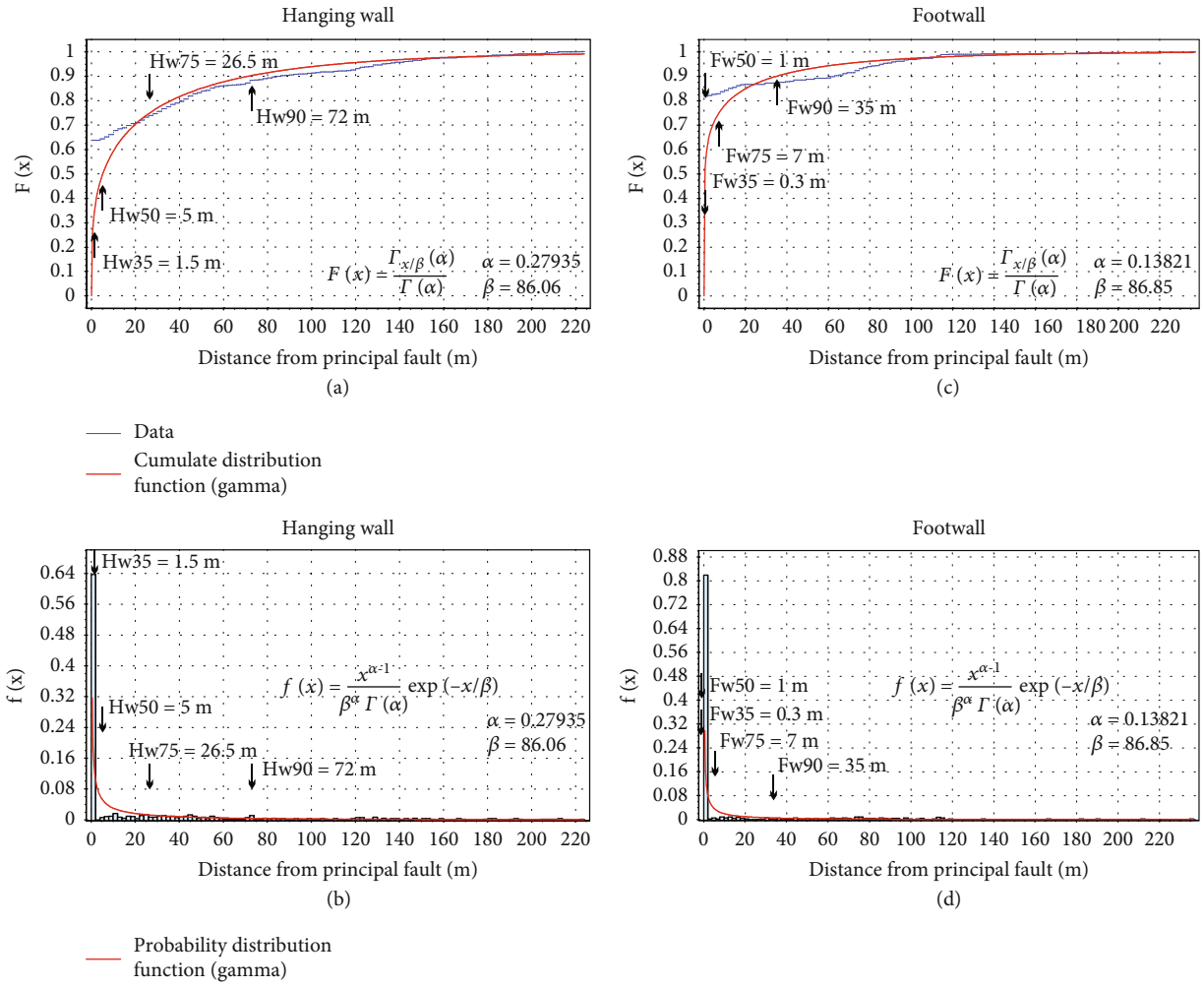

Probability	Total-RZW	FW-RZW	HW-RZW	FW : HW
90 %	107 m	35 m	72 m	1 : 2
75 %	33.5 m	7 m	26.5 m	1 : 3.8
50 %	6 m	1 m	5 m	1 : 5
35 %	1.8 m	0.3 m	1.5 m	1 : 5

(e)

Figure 11: Rupture zone width cumulative function and probability density function obtained by using the EasyFitProfessional software vers. 5.5 at the HW of the P-CoRs (a, b) and at the FW of the P-CoRs (c, d). (e) Results of the analysis for probabilities of 90, 75, 50, and 35% for the total-, FW-, and HW-RZW. The ratios (FW : HW) are also reported.

RZW is large independent of CoRs or Qfs VS values (Figures S10a and S10b). In general, D-CoRs tend to be distant from the P-CoRs as the CoRs and Qfs VSs increase. CoRs and Qfs Vs correlate well, as shown in Figure S10c, suggesting a general correlation, between the behavior of the 1983 and earlier earthquakes.

Analyzing the surface deformation only in terms of VS, interesting points of discussion are highlighted by the along-strike profiles (Figure 6). The reconstructed configuration is characterized by a complex along-fault sinuosity with variable displacement. This alternation of ruptured and unruptured segments is a feature recognized worldwide (e.g., [72, 73]) and considered classic for mature faults [74, 75].

Coseismic VS profiles with triangular and asymmetric shapes are a generic feature. Manighetti et al. [72, 76] showed that triangular slip profiles are self-similar based on a large worldwide database. All profiles have a zone of maximum slip or major asperity. Based on the distance between the hypocenter and maximum slip, they concluded that earthquakes generally nucleate at a distance from the maximum slip at 20–30% of total rupture length. This is the "asperity size" and is structurally defined. To compare our data with other studies, we normalized the VS and distance values to the maximum and average values and compared the profiles with the results from Manighetti et al. [72] (all kinematics), Wesnousky [1] (normal faulting), and Brozzetti et al. [30] (2016-2017 central Italy seismic sequence). A good correspondence between these profiles can be observed in Figure S11, supporting the results of these authors.

3.2. Segmentation Pattern of the Borah Peak Earthquake. As mentioned above, the segmentation of a fault is done considering factors generically described as "irregularities," described by Yeats et al. [62] who states: "*These irregularities permit a long fault to be divided into segments. Segments based on geology may correspond to earthquake rupture zones, permitting a forecast of the moment magnitude of a future earthquake. Geological discontinuities that have been shown to be segment boundaries include large en-échelon stepovers, gaps in faulting, salients, sharp changes in fault strike, and zones of great structural complexity. However, some segment boundaries may be "leaky"; earthquake rupture may cross these boundaries in some cases but not others. A segment boundary may stop a small earthquake, but not a very large one.*"

We study the segmentation of the Warm Springs and Thousand Springs segments and Arentson Gulch Fault (Figure 12(a)). Some of the discontinuities that we have highlighted as "major complexities" have been described by previous authors. In particular, these researchers segmented the entire structure in six segments based on changing geomorphic expression, structural relief, and age of last movement by dating faulted soils (Figure 1) [6, 7, 44–48, 77]. DuRoss et al. [7] examined the branching Arentson Gulch Fault on the 1983Eq rupture and the two most recent paleoearthquakes [49]. The two previous paleoearthquakes resulted in different slip patterns with moment release concentrated along the 15 km-long Warm Springs Segment. The most recent paleoearthquake (6-7 ka) primarily ruptured the Warm Springs Segment, the Arentson Gulch Fault, and possibly the northern portion of the Thousand Springs Segment with diminished slip. The earlier paleoearthquake (<~15 ka) ruptured the Warm Springs Segment and terminated just north of Willow Creek Hills. Using these three earthquake rupture patterns, they conclude that the Arentson Gulch Fault acts as a nonpersistent barrier that occasionally allows for full-displacement ruptures to pass through but that often modulates the rupture length and surface faulting on a subsequent fault segment. DuRoss et al. [7] interpret the Willow Creek Hills area as a structural complexity that divides two segments due to presence of Qfs and the absence of 1983Eq-related ruptures in the gap area (DuRoss et al., 2019, their Figure 11). Boncio et al. [71] highlights the presence of structural complexities at West Spring Block (1 km NW of Doublespring Pass road) along the Thousand Springs Segment where the fault bends sharply and the RZW is large (Figures 3(c) and 8(b)).

To describe the segmentation of the study area, we used surface faulting data (i.e., CoRs VS, Qfs VS, RZW, geometric and structural complexities, and kinematic partitioning), numerically weighing each of the features identified based on their magnitude. We first reported the mapped RZW and individual geometric-structural complexities (Figure 12(a)) that are numbered corresponding to Table S1, which also includes a brief description of the features at each site.

We integrated the fault-slip data by adding the T-axes of the deformation from the kinematic analysis (Figure 12(b)) and used the envelope curves from the VS profiles (Figure 12(c)). We compare the CoRs and Qfs VS, RZW, and sense of slip.

Sharp fault bends, intersections with cross-structures, underlapping and overlapping en-échelon arrangements, and gaps between aligned faults are considered as likely barriers to rupture. Wesnousky [78] and Biasi and Wesnousky [79, 80] relate the presence and size of gaps and steps to the propagation of the surface rupture and when the rupture likely stops. However, this research mostly refers to the major discontinuities and therefore to the higher levels relative to our segmentation (discussed below). The identification of the minor levels of segmentation is important since, as shown by previous studies in similar seismotectonic contexts (e.g., Brozzetti et al. [30] for the 2016-2017 central Italy seismic sequence), these minor levels (i.e., 1-4 km-long) exert strong control on the slip distribution. Therefore, their identification and study are fundamental to anticipate the distribution of fault slip, a prerequisite for seismic hazard assessment.

We parameterize and present all the observations in Table 2. We divided the portions of the LRF that ruptured in 1983 into four levels of segmentation. These levels and lengths are mostly consistent with much of the literature on segmentation (e.g., [2, 30, 40, 81–83]). The first level corresponds to the segments (i.e., Thousand Springs and Warm Springs). The second-level has "sections" (I-VI) with 8-10 km lengths. In the third level are "subsections" (1-9) consisting of fault portions with similar characteristics and lengths of 4-6 km. The smallest levels of segmentation are "sectors" (e.g., 1a, 1b, 1c) with an average length of 2 km and ranging from 1.5 to 4 km and are constrained from our high resolution data.

Based on the intersections of the lower segmentation levels, we report in Table 2 the VS variations (which correspond to negative peaks) both for the CoRs and for the Qfs, obtaining the values from the analysis of the VS along-strike. These variations are divided based on their magnitude, described in the previous sections of this paper and here reported: 1st order = $30 < \Delta VS < 80$; 2nd order = $90 < \Delta VS < 130$; 3rd order = $\Delta VS > 130$. We, therefore, indicate if the intersection between the sectors corresponds to the tip of the coseismic deformation, which is therefore indicated only with a check and is always arbitrarily defined as a first-order factor.

We then introduced the parameter of kinematic partitioning (i.e., T-axis trend variations) also divided into three orders of magnitude (ΔT): 1st order = $15° < \Delta T < 25°$; 2nd order = $25° < \Delta T < 40°$; 3rd order = $\Delta T > 40°$. We subsequently reported the sudden variations in RZW and the strike variations (e.g., bends), divided, respectively, as follows: ΔRZW, in meters (1st order = $\Delta RZW < 100$; 2nd order = $100 < \Delta RZW < 150$; 3rd order = $\Delta RZW > 150$) and ΔStrike (1st order = $\Delta Strike < 20°$; 2nd order = $20° < \Delta Strike < 30°$; 3rd order = $\Delta Strike > 30°$. Finally, we report the gaps and stepovers, classified as follows: gaps (m) among CoRs: 1st order = gap < 100; 2nd order = 100 < gap < 300; 3rd order = gap > 300.

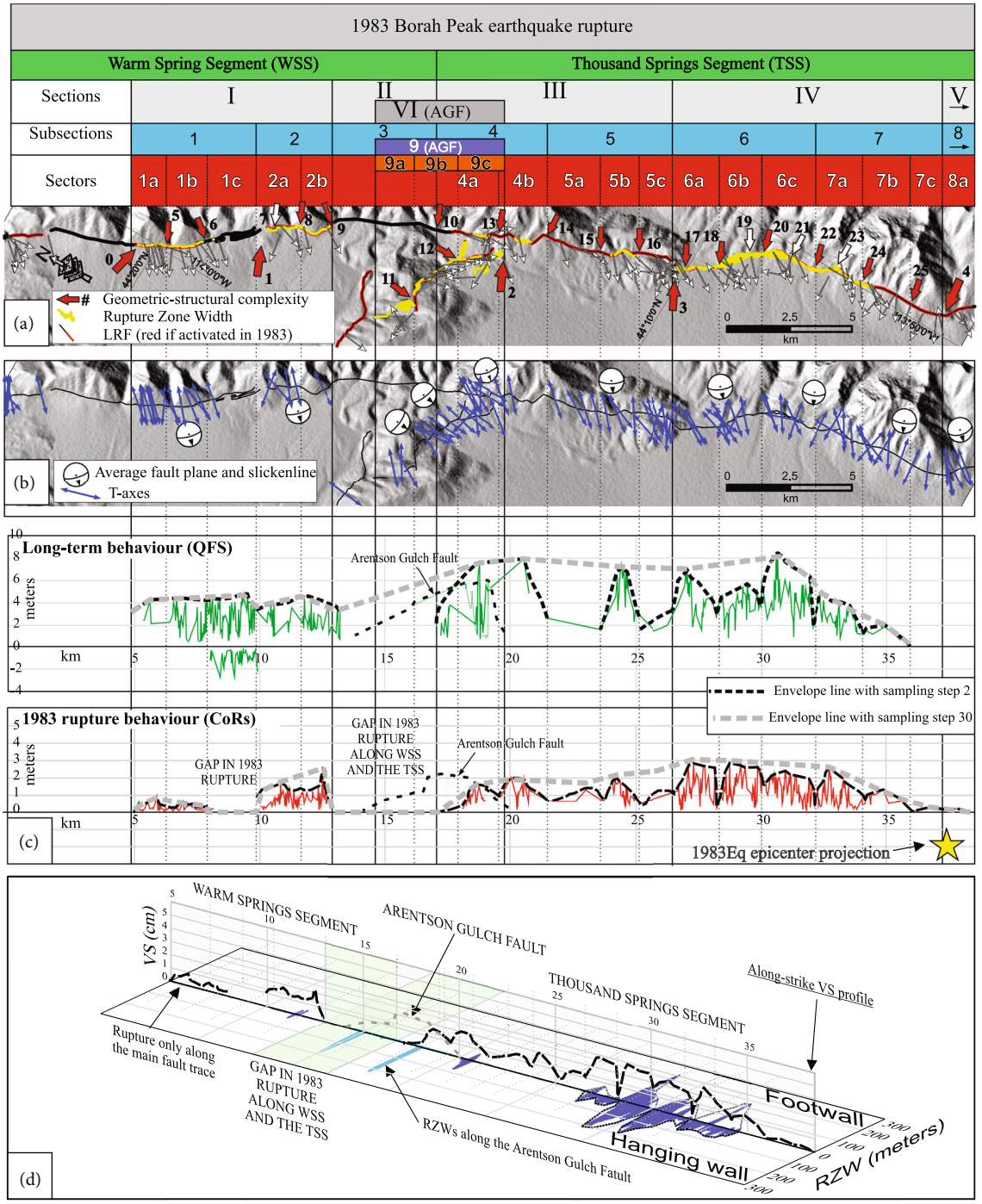

FIGURE 12: Full integration of data analyzed in this paper. The upper portion of the figure shows the segmentation orders with different colors. (a–c) are interconnected and the segmentation is marked by vertical solid (sections) and dotted (subsections and sectors) lines. (a) Slip vectors (thin white arrows), RZWs (yellow polygons), and geometric-structural complexities (bold white or red arrows) mapped along the Arentson Gulch Fault, Thousand Springs Segment, and Warm Springs Segment. Arrows indicating the complexities are red if correspond to a segmentation boundary and white if not. Numbers close to these arrows indicate the ID of the geometric-structural complexity reported in the supplementary Table S1, where a synthetic description of each location indicated is provided. (b) *T*-axes of the strain (blue arrows) and average fault planes and slickenlines represented with stereoplots. (c) Long-term (upper graph) and 1983 (lower graph) rupture behavior along the Thousand Springs Segment, Warm Springs Segment, and Arentson Gulch Fault. Black and grey curves are the envelopes obtained from the VS analysis with sampling steps 2 and 30, respectively. Green and red lines correspond to the Qfs and CoRs VS integrated measurements, respectively (as reported in Figures 6(a), 6(b), and 6(d)). The yellow star is the projection of the 1983 mainshock considering the trend of the seismogenic source parallelogram in Richins et al. [10, their Figure 7]. (d) 3D model comparing the CoRs-VS envelopes (in cm) and the FW- and HW-RZW (in m).

Table 2: Factors controlling the segmentation of the 1983 Borah Peak earthquake. We report segments, sections, and subsections as described in the text. Sectors are reported considering the boundaries among each other. The factors controlling the segmentation are reported based on their magnitude (i.e., first, second, and third order) as described in the main text. The scoring shows how many first, second, and/or third order have been assigned to each sector's intersection. According to the weight of each order assigned, the weighted total is calculated. The weighted totals in gray boxes correspond to the boundaries between the highest levels of the segmentation.

Segments	Warm Springs Segment						Arentson Gulch Fault		Thousand Springs Segment												
Sections	I					II	VI		III				IV								V
Subsections	1		2			3	9		4		5			6			7				8
Boundaries between sectors	1a - 1b	1b – 1c	1c - 2a	2a - 2b	2b - 3	3 - 4a	9a - 9b	9b - 9c	9c - 4a	4a – 4b	4b – 5a	5a - 5b	5b – 5c	5c - 6a	6a - 6b	6b - 6c	6c - 7a	7a - 7b	7b - 7c	7c - 8a	
Negative CoRs VS peak (Δ in m)	0.8		1.3		2	1.8	0.8	0.5		1.3	1.5	1.3	1.5	2	2.5	1.2	2.2	1.3	0.9	0.3	
Negative Qfs VS peak (Δ in m)	0.5	1	1.5		1.8	2					3	5	2	4	1	3	4	2.2	2	ND	
Tip of the 1983 coseismic deformation		✓	✓		✓	✓			✓											✓	
Kin. partitioning (T-axes trend Δ, Deg)	±25		±40		ND	ND	±40	±10	±45	±35	±10	±15	±35	±45	±25	±15	±30	±30		±45	
RZW variation (Δ in m; ✓ if close to gaps)		✓	✓	100	✓	✓	400	1500	ND	ND	ND	ND	630	230	150	350	130	100	ND	360	
Sharp bend (strike Δ, Deg)	15		25	40	40	10	15	25	45	35	60			50	20	15	25	25		40	
Gap among ruptures (m)		2700		55	4500		295		500	ND	ND	ND	ND	500		50	60	ND	ND	NA	
Overlapping or underlapping en ´echelon arrangements (*e.g.*, stepovers)			✓	✓			✓		✓		ND	ND	✓	✓	✓		✓	✓	ND	✓	
ND/NA	0	0	0	0	1	3	0	0	2	4	5	5	1	0	0	0	0	1	5	6	
First-order (weight: x1)		2	6	1	6	5	2	1	5	2	3	2	4	6	1	3	2	2	1	5	
Second-order (weight: x0.75)		1	2	0	0	0	2	1	0	1	0	0	1	1	3	0	3	3	1	0	
Third-order (weight: x0.5)	4	0	0	3	0	1	2	2	0	0	1	1	0	0	2	3	2	1	0	1	
Weighed Total	*2*	*2.75*	*7.5*	*2.5*	*6*	*5.5*	*4.5*	*2.75*	*5*	*2.75*	*3.5*	*2.5*	*4.75*	*6.75*	*4.25*	*4.5*	*5.25*	*4.75*	*1.75*	*5.5*	

Based on the order assigned to each value (1st, 2nd, or 3rd order described above), we performed a weighted scoring, assigning each 1st order a weight equal to 1, each 2nd order a weight equal to 0.75, and each 3rd a weight equal to 0.5. Note that some intersections between sectors score higher than others. These boundaries also divide subsections and sections (Table 2).

The factors reported and used in this work are related to each other; this is not surprising given their relationship to the 1983 rupture pattern. In other cases, however, these overlapping factors are interesting and noteworthy. Interesting results have been shown over time in relating displacement and throw rates along normal faults to geometric complexities, in particular at strike changes, or bends. Close to changes in fault orientation, the displacement changes too, as required to accommodate a uniform slip vector [84–86]. This agrees with what was observed in our work. In fact, the bend present along section IV of Thousand Springs Segment, and in particular between sectors 6b and 6c, corresponds to the maximum VS during the 1983Eq. This arcuate and concave shape towards the FW (Supplementary Material Figure S6) consists of 2 minor bends (sectors 6b and 6c). This shape is described by Wu and Bruhn [87] as a growth style of some normal faults in Utah (USA), but with opposite convexity and concavity to those of sectors 6b and 6c of the LRF. Probably, the different scale causes difference, although Wu and Bruhn [87] consider these structures to be self-similar.

The subsections with the largest VS measurements have the most distributed deformation along the HW and FW (Figure 12(d)). The RZW is also related to kinematic partitioning. Ferrario and Livio [88] illustrated that distributed faulting is controlled by geological factors such as rock type and fault geometry, while Boncio et al. [71] proposed that changes in fault rake modulate RZW. Figure 12(b) shows that subsections 4, 5, 6, 7, 8, and 9 are characterized by a general northwards rotation of the *T*-axes. These axes show that the oblique component of deformation gradually increased northward during the northward rupture propagation of the 1983Eq (see also Figure S8 and Table 1). RZW values increase northwards along subsections 8, 7, 6, and 5 (see Figure 3) with the peaks in subsections 6, 5, and 9. Section I has purely dip-slip deformation and the lowest RZW. We consider these *T*-axes and RZW as related, consistent with Boncio et al. [71] and von Hagke et al. [43] who identify the oblique component along normal faults as a likely cause of HW strain partitioning and the RZW increase.

As shown in Table 2, RZW variation occurs near geometric complexities such as stepovers. This observation explains the simple geometric relationship between adjacent CoRs ([89] and references therein) and that the RZW is directly related to the transfer of slip between neighboring structures and at fault bends. Along strike and depth-dependent variations in soil rheology and rock type that are crossed by the slip in its propagation can impact the RZW (e.g., [30, 89–91], and references therein). Zinke et al. ([92] among others) show the structural fault maturity and the type of near-surface material through which the rupture propagates control off-fault deformation. Future research including detailed geological mapping and the comparison of pre- and post-rupture datasets along the LRF could address variations in factors such as the RZW (e.g., [90, 93–95]).

Having developed the detailed segmentation, we parameterize the sectors, subsections, and sections. We provided detailed information including location, length, strike, dip-direction, and rake in Table 3. We established the maximum, minimum, and average VS and RZW values on each sector calculated the ratios between the two maximum values, showing that areas with larger VSs have wider RZWs.

To provide the full information about sector location, we mapped each sector following the P-CoRs trace from Bello et al. [8]. In areas where high-resolution data were not available, we mapped the sectors along the LRF trace from the USGS [54]. We provide the mapped faults as a shapefile (Supplementary Material Data S2) with an attribute table with the information in Table 3.

Using the mean VS of each of the orders we reconstructed, we calculated the surface deformation accommodated during 1983Eq by the individual sectors as a function of distance along the fault trace (Table 3). An interesting partitioning of the deformation is seen in the cumulative deformation along the individual section, subsection, and sector. Section I accommodates 18.4% of the surface deformation, subsection 1 accommodates 4.7%, and subsection 2 accommodates 13.7%. Given that section II is a gap in the 1983 rupture (Figure 12), the 18.4% of section I is all of the deformation accommodated by the Warm Springs Segment. In contrast for Thousand Springs Segment, Section III accommodates 29.3% of the deformation, and section IV accommodates 38.1%. Sections III and IV accommodate 67.4% of the deformation together, and section V accommodates 1.1%. The 68.5% is therefore the total deformation accommodated by Thousand Springs Segment. Finally, section VI accommodates 13.1% of the surface deformation.

In summary, we show that ~69%, 18%, and 13% of surface deformation accommodated by Thousand Springs Segment, Warm Springs Segment, and Arentson Gulch Fault, respectively. DuRoss et al. [7] found similar results: the Thousand Springs Segment, Warm Springs Segment, and the Arentson Gulch Fault contributed to 80%, 9%, and 11%, respectively, of the 1983 moment release. Despite the precise differences in quantities measured, the similarity is interesting as it correlates the moment released with the deformation at the surface. It would be even more similar if the rupture gap in Warm Springs Segment (section II) was excluded from the calculation.

We provide a summary of the segmentation and the single section parameters used in the analysis of seismic hazard in Figure 13. We also synthesized the results of the kinematic analysis from the surface deformation data (represented in the contour of the *T*-axis of the deformation in stereoplots). Note the gradual increase in the left-lateral component northward from section V to section VI.

Table 3: Summary table of segmentation. The values in the table refer to the sectors, except for the last column. Seg: segment; Sec: section; Sub sec: subsection; *X*-start, *X*-end, *Y*-start, *Y*-end coordinated of the sectors. Elev: elevation; Dip dir: dip direction. Rake is in Aki-Richards's format. VS_{max}: maximum VS along the sector. VS_{min}: minimum VS along the sector. VS_{mean}: average VS along the sector. RZW_{max}: maximum RZW along the sector. RZW_{min}: minimum RZW along the sector. RZW_{mean}: average RZW along the sector. StD: VS standard deviation. VS: RZW: ratio between VS and RZW. % sector: surface deformation accommodated by the sector intended as a function of distance along the fault trace in percentage. % subsections: surface deformation accommodated by the section intended as a function of distance along the fault trace in percentage.

Seg	Sec	Sub sec	Sector	*X*-start	*X*-end	*Y*-start	*Y*-end	Elev	Length	Strike	Dip dir	Rake	VS_{max}	VS_{min}	VS_{mean}	RZW_{max}	RZW_{min}	RZW_{mean}	StD	VS : RZW	% sector	% subsection
WSS	I	1	1a	-113.9974	-114.0064	44.3302	44.3415	2195	1.5	155	245	-90.0	98	6	27.9	—	—	—	23.0	—	2.4	
WSS	I	1	1b	-113.9862	-113.9974	44.3200	44.3302	2177	1.5	145	235	-86.6	64	6	27.5	—	—	—	14.5	—	2.3	4.7
WSS	I	1	1c	-113.9668	-113.9845	44.3070	44.3187	—	2.0	143	233	-90.0	0	0	0	0	0	0	0.0	—	0	
WSS	I	2	2a	-113.9545	-113.9636	44.2930	44.3034	2361	1.5	153	243	-90.0	174	21	74	48	8	30	38.0	1 : 27.6	6.2	13.7
WSS	I	2	2b	-113.9440	-113.9546	44.2839	44.2927	2350	1.5	135	225	-90.0	266	15	92	—	—	—	46.0	—	7.5	
WSS	II	3	3	-113.9200	-113.9440	44.2508	44.2839	—	4.2	155	245	—	0	0	0	0	0	0	0.0	—	0	0
TSS	III	4	4a	-113.9063	-113.9200	44.2304	44.2508	2484	2.8	155	265	-72.7	146	55	86	45	7	19	30.0	1 : 31	3.9	9.5
TSS	III	4	4b	-113.8940	-113.9063	44.2169	44.2304	2573	2.1	140	230	-90.0	194	14	92.4	115	5	48	47.7	1 : 59	5.6	
TSS	III	5	5a	-113.8866	-113.8937	44.1971	44.2164	—	2.3	167	257	-68.9	133	55	90.0	—	—	—	31.3	—	5	
TSS	III	5	5b	-113.8793	-113.8865	44.1846	44.1966	2142	1.6	160	250	-82.0	208	34	111.8	42	12	29	44.7	1 : 20	8.7	19.8
TSS	III	5	5c	-113.8729	-113.8768	44.1697	44.1847	—	1.8	175	265	-79.0	130	30	87.6	—	—	—	36.8	—	6.1	
TSS	IV	6	6a	-113.8616	-113.8728	44.1574	44.1696	2153	1.7	130	220	-89.4	295	13	140.9	133	6	43	82.0	1 : 45	10.4	
TSS	IV	6	6b	-113.8447	-113.8616	44.1460	44.1570	2189	2.0	120	210	-85.2	286	26	141.2	291	9	130	67.2	1 : 102	8.9	27
TSS	IV	6	6c	-113.8378	-113.8442	44.1279	44.1457	2213	2.2	170	260	-88.9	241	9	137.2	298	7	111	60.6	1 : 124	7.7	
TSS	IV	7	7a	-113.8319	-113.8377	44.1109	44.1273	2392	2.1	150	240	-84.9	263	16	92.7	194	5	52	60.8	1 : 74	5.5	
TSS	IV	7	7b	-113.8276	-113.8324	44.0917	44.1108	2385	2.3	175	265	-89.9	105	43	72.6	80	9	36	24.8	1 : 76	4.1	11.1
TSS	IV	7	7c	-113.8242	-113.8276	44.0802	44.0917	—	1.3	167	257	-90.0	30	5	15.7	—	—	—	10.5	—	1.5	
TSS	V	8	8a	-113.8121	-113.8242	44.0718	44.0802	—	1.4	135	225	-90.0	21	5	12	—	—	—	6.7	—	1.1	1.1
AGF	VI	9	9c	-113.9100	-113.9272	44.2263	44.2390	2279	2.0	135	225	-92.4	163	18	82	224	192	207	53.0	1 : 137	5.1	
AGF	VI	9	9b	-113.9186	-113.9591	44.2401	44.2420	2293	3.8	110	200	-67.3	227	29	143	182	6	90	51.0	1 : 80	4.9	13.1
AGF	VI	9	9a	-113.9562	-113.9732	44.2443	44.2531	2276	1.8	125	215	-87	89	18	44	356	44	268	19.8	1 : 400	3.1	

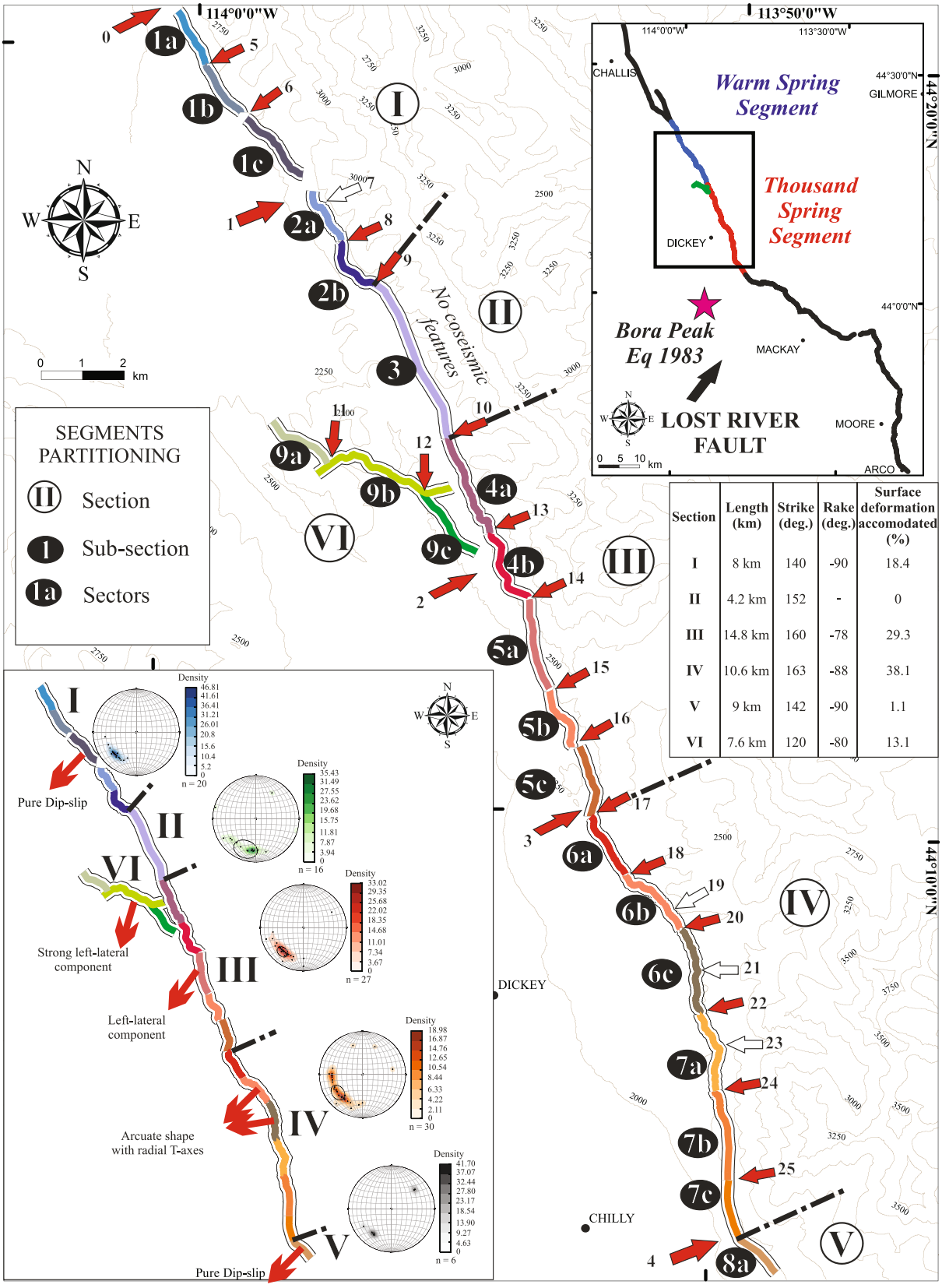

Section	Length (km)	Strike (deg.)	Rake (deg.)	Surface deformation accomodated (%)
I	8 km	140	-90	18.4
II	4.2 km	152	-	0
III	14.8 km	160	-78	29.3
IV	10.6 km	163	-88	38.1
V	9 km	142	-90	1.1
VI	7.6 km	120	-80	13.1

FIGURE 13: Synthetic representation of the segmentation obtained. Dotted and dashed lines are section boundaries. Sectors are represented with different shades of red, blue, and green for the Thousand Springs Segment, Warm Springs Segment, and Arentson Gulch Fault, respectively. Solid background green lines are 250 m contour lines. In the inset table, section parameters are reported. The results of the kinematic analysis from the surface deformation data are represented in the contour of the *T*-axis of the deformation in stereoplots.

4. Conclusions

In light of new geological-structural data presented here and available in recent literature, thanks to improvements in small Unmanned Aerial Vehicles (sUAV) technology and Structure-from-Motion (SfM) processing techniques, we present an integrative study on the 1983 Borah Peak earthquake, which takes into account a complete bibliography dating back to the 80s and 90s of the last century and new (last few years) datasets available.

The original results here presented are summarized as follows.

(1) The 1983Eq generated a complex pattern of surface deformation, with a total of over 51 km of P- and D-CoRs traces generally less than 150 meters long. They strike ~N140 (synthetic) and ~N290 (antithetic) but with a systematic variation of approximately 20° between HW and FW, thus suggesting a direct control over the deformation by the location with respect to the main trace. The 1983 and long-term VS measurements and RZW were analyzed and outline a complex along-strike evolution, with well-detailed positive and negative peaks. We find a positive correlation between CoRs and Qfs VS, that suggests a similar behavior of the 1983 surface deformations and the long-term deformations. The major VSs are along the CoRs striking ~N160.

(2) The presence of large deformation zones distributed along the HW and FW (D-CoRs) of the main faults (P-CoRs) is a topic little addressed in the literature [96] but plays an important role in the fault displacement hazard assessment. We suggest not to underestimate these features as, according to our analyses, they accommodate a large portion of the strain both in terms of length (~19.5 km) and VS (~66% of the total VS produced along the Thousand Springs Segment). This behavior should be taken into consideration for hazard studies as well as for the development of seismic microzonation protocols of urbanized areas, increasingly applied in various countries of the world.

(3) 47.2% of the D-CoRs is located at the HW, 9.4% at the FW, and 43.4% represents the P-CoR. However, we observe areas where the deformation is more distributed and areas where it concentrates along a single rupture (southern and northern portions of the fault, respectively). Areas with wider RZWs are also the areas with the largest VS peaks, both for long-term and 1983 behaviors. By calculating the ratios applying the probability density functions, we confirm an average ratio of about 1 : 4 (FW : HW), consistent with the deformation patterns in active normal faults environments (e.g., Boncio et al. [71]), even if it can change from 1 : 2 to 1 : 5. Therefore, we suggest caution in applying territorial planning constraints based on probability calculations in other areas of the world.

(4) New fault-slip data show a kinematic partitioning throughout the 1983Eq epicentral area. From an analysis of the T-axis of the deformation, we show that the kinematics have a gradually increasing left-lateral component from the southern tip of Thousand Springs Segment towards the northern tip. We hypothesize that this kinematic partitioning exerts direct control over the RZW. Along the Arentson Gulch Fault, we find the maximum left-lateral components of displacement and some of the major peaks of RZW. The Warm Springs Segment shows almost purely dip-slip kinematics and RZW almost everywhere equal to zero.

(5) We show the presence of geometric-structural complexities along the segments of the LRF activated in 1983, such as gaps, stepovers, and bifurcations, which have been divided into minor and major complexities. These complexities, extensively described by a large literature, represent important features in describing the surface deformation and segmentation pattern. We highlight an interesting arcuate shape, concave towards the FW, present along section IV of Thousand Springs Segment, which shows the control of the geometry on the deformation. As suggested in previous literature (theoretical or applied to other areas of normal active faulting) [84–86], bends and strike changes make the VS increase to accommodate a uniform slip vector.

(6) Our methodological approach integrates a large dataset of quality-selected vertical separation data (both 1983Eq and long-term), combined with RZW measurements, new fault/slip data, and an analysis of major and minor structural-geometric complexities. This allowed to divide the portions of the LRF that released the 1983Eq into 4 orders of segmentation: a first-order "segment", a second-order "section" (I–VI, each 8-10 km-long), a third-order "subsection" (1–9, 4 to 6 km-long), and a fourth-order "sector" (1a-9c, 1.5 to 4 km-long). The magnitudes of these orders agree with those of the segmentations applied in other areas of the world, but thanks to the high detail achieved with the data at our disposal, we augmented the orders by adding the "sectors." The same degree of detail should be achieved in other areas for which high-quality data are available, to improve knowledge on coseismic surface rupture segmentation.

(7) We calculate that section I accommodated the 18.4% of the surface deformation, II the 0%, III the 29.3%, IV the 38.1%, V the 1.1%, and VI the 13.1%. Overall, these data are consistent with DuRoss et al. [7] which calculates that the Warm Springs Segment and the Arentson Gulch Fault contributed to 9% and 11%, respectively, of the total moment release of the 1983 earthquake. This positive correlation between the total moment release and surface deformation is an interesting result that could motivate future research.

The results of this study can help to understand how and if the total displacement of a given fault segment may be partitioned in discrete displacement sublevels, with a fixed characteristic fault length and with slip proportional to earthquake magnitude. Furthermore, it may help identify fault portions more prone to intense surface breaking. In other words, the outcropping along-fault variability in the preexisting damage zone may represent a dominant factor in controlling the earthquake slip distributions, with evident implications for seismic hazard evaluations. The proposed segmentation, more detailed and comprehensive than those previously described, provides new constraints for paleoseismic and seismotectonic studies, together with new useful details on the effects of this important earthquake that can be used for new static stress calculations and seismic hazard assessment computations of similar earthquakes worldwide.

Data Availability

The original contributions presented in the study are included in the article/supplementary material.

Conflicts of Interest

The authors declare that they have no conflicts of interest.

Acknowledgments

The authors are thankful to the editor and reviewers for their thoughtful review that improved this manuscript. This research was supported by DiSPUTer Department funds and by funds from the School of Advanced Studies G. d'Annunzio at University of Chieti-Pescara (Italy) to the "Earthquake and Environmental Hazards" Ph.D. Course. We acknowledge Petroleum Experts that provided the Move 2019.1 suite software license.

Supplementary Materials

In the Supplementary Materials, we provide a figure showing the methodological workflow of this paper (Figure S1); the distribution of the data selected from Bello et al. [8] of the areas 3, 4, 5, 6, 7, and 9, on the hillshade produced with the SfM [49, 55] (Figures S2 - S4); a figure representing a 3D model that shows the complex surface rupture pattern produced by the 1983 Borah Peak earthquake (Figure S5); a panel in which we compare all the complexities found and observable along the two segments responsible for 1983 earthquake with the models (block diagrams) classically known in the (to be read in A3 format; Figure S6); a figure showing the pseudofocal mechanisms obtained from the kinematic analysis of the fault/slip data and their parameters (Figure S7); three figures showing graphs and plots of geometric and statistical properties of the data analyzed in this paper (Figures S8 to S10); a figure comparing the VS data used in this paper with global earthquakes. We also provide a shapefile containing the fault/slip data used (Supplementary Data 1) and a shapefile with the fault traces mapped according to the segmentation obtained in this paper, both reporting information in the attribute table (Supplementary Data 2). *(Supplementary Materials)*

References

[1] S. G. Wesnousky, "Displacement and geometrical characteristics of earthquake surface ruptures: issues and implications for seismic hazard analysis and the process of earthquake rupture," *Bulletin of the Seismological Society of America*, vol. 98, no. 4, pp. 1609–1632, 2008.

[2] A. Valentini, C. B. DuRoss, E. H. Field et al., "Relaxing segmentation on the Wasatch fault zone: impact on seismic hazard," *Bulletin of the Seismological Society of America*, vol. 110, no. 1, pp. 83–109, 2020.

[3] E. M. Baldwin, "Faulting in the lost river range area of Idaho," *American Journal of Science*, vol. 249, no. 12, pp. 884–902, 1951.

[4] K. L. Johnson, E. Nissen, and L. Lajoie, "Surface rupture morphology and vertical slip distribution of the 1959Mw7.2 Hebgen Lake (Montana) earthquake from airborne lidar topography," *Journal of Geophysical Research: Solid Earth*, vol. 123, no. 9, pp. 8229–8248, 2018.

[5] L. M. Liberty, Z. M. Lifton, and T. D. Mikesell, "The 31 March 2020 M_w 6.5 Stanley, Idaho, earthquake: seismotectonics and preliminary aftershock analysis," *Seismological Research Letters*, vol. 92, 2021.

[6] A. J. Crone, M. N. Machette, M. G. Bonilla et al., "Surface faulting accompanying the Borah Peak earthquake and segmentation of the Lost River fault, central Idaho," *Bulletin of the Seismological Society of America*, vol. 77, pp. 739–770, 1987.

[7] C. B. DuRoss, M. P. Bunds, R. D. Gold et al., "Variable normal-fault rupture behavior, northern Lost River fault zone, Idaho, USA," *Geosphere*, vol. 15, no. 6, pp. 1869–1892, 2019.

[8] S. Bello, C. P. Scott, F. Ferrarini et al., "High-resolution surface faulting from the 1983 Idaho Lost River fault M_w 6.9 earthquake and previous events," *Scientific Data*, vol. 8, no. 1, p. 68, 2021.

[9] C. W. Stoven, "Isoseismal map and intensity distribution for the Borah Peak, Idaho, earthquake of October 28, 1983," in *Proceedings of Workshop XXVIII on the Borah Peak, Idaho, Earthquake*pp. 401–408, Menlo Park, California, 1985.

[10] S. M. Jackson and J. Boatwright, "Strong ground motion in The 1983 Borah Peak, Idaho, earthquake and its aftershocks," *Bulletin of the Seismological Society of America*, vol. 77, no. 3, pp. 724–738, 1987.

[11] J. Boatwright, "Characteristics of the aftershock sequence of the Borah Peak, Idaho, earthquake determined from digital recordings of the events," *Bulletin of the Seismological Society of America*, vol. 75, no. 5, pp. 1265–1284, 1985.

[12] D. I. Doser and R. B. Smith, "Source parameters of the 28 October 1983 Borah Peak, Idaho, earthquake from body wave analysis," *Bulletin of the Seismological Society of America*, vol. 75, no. 4, pp. 1041–1051, 1985.

[13] S. E. Barrientos, R. S. Stein, and S. N. Ward, "Comparison of the 1959 Hebgen Lake, Montana and the 1983 Borah Peak, Idaho, earthquakes from geodetic observations," *Bulletin of the Seismological Society of America*, vol. 77, pp. 784–808, 1987.

[14] J. Nabelek, H. Eyidogan, and M. N. Toksoz, "Source parameters of the Borah Peak, Idaho earthquake of October 28, 1983

from body-wave inversion," *EOS, tTransactions of the American Geophysical Union*, vol. 66, no. 308, 1985.

[15] G. Ekstrom and A. M. Dziewonski, "Centroid-moment tensor solutions for 35 earthquakes in western north America (1977-1983)," *Bulletin of the Seismological Society of America*, vol. 75, no. 1, pp. 23–39, 1985.

[16] US Geological Survey, "Search earthquake catalog," September 2020, https://earthquake.usgs.gov/earthquakes/search/.

[17] G. Pang, K. D. Koper, M. C. Stickney et al., "Seismicity in the Challis, Idaho, Region, January 2014-May 2017: late aftershocks of the 1983 Ms 7.3 Borah Peak earthquake," *Seismological Research Letters*, vol. 89, no. 4, pp. 1366–1378, 2018.

[18] R. E. Wallace, M. G. Bonilla, and H. A. Villalobos, *Faulting related to the 1915 earthquakes in Pleasant Valley, Nevada*, Geological Survey professional paper, 1274 A-B, 1984.

[19] J. Ren, X. Xu, S. Zhang et al., "Surface rupture of the 1933 M 7.5 Diexi earthquake in eastern Tibet: implications for seismogenic tectonics," *Geophysical Journal International*, vol. 212, no. 3, pp. 1627–1644, 2018.

[20] D. I. Doser, "Earthquake processes in the Rainbow Mountain-Fairview Peak-Dixie Valley, Nevada, region 1954–1959," *Journal of Geophysical Research*, vol. 91, no. B12, pp. 12572–12586, 1986.

[21] M. M. Clark and J. C. Yount, "Surface faulting along the Hilton Creek fault associated with Mammoth Lakes, California, earthquakes of May 1980," *Seismological Society of America, Earthquake Notes*, vol. 52, pp. 45-46, 1981.

[22] S. Bello, R. de Nardis, R. Scarpa et al., "Fault pattern and seismotectonic style of the Campania–Lucania 1980 earthquake (M_w 6.9, Southern Italy): new multidisciplinary constraints," *Frontiers in Earth Science*, vol. 8, article 608063, 2021.

[23] J. A. Jackson, J. Gagnepain, G. Houseman et al., "Seismicity, normal faulting, and the geomorphological development of the gulf of Corinth (Greece): the Corinth earthquakes of February and March 1981," *Earth and Planetary Science Letters*, vol. 57, no. 2, pp. 377–397, 1982.

[24] M. J. Pender and T. W. Robertson, "Edgecombe earthquake," *Bulletin of the New Zealand National Society for Earthquake Engineering*, vol. 20, no. 3, pp. 201–249, 1987.

[25] H. S. Akyüz, R. Hartleb, A. Barka et al., "Surface rupture and slip distribution of the 12 November 1999 Duzce earthquake (M 7.1), north Anatolian fault, Bolu, Turkey," *Bulletin of the Seismological Society of America*, vol. 92, no. 1, pp. 61–66, 2002.

[26] M. Furuya and T. Yasuda, "The 2008 Yutian normal faulting earthquake (Mw 7.1), NW Tibet: non-planar fault modeling and implications for the Karakax fault," *Tectonophysics*, vol. 511, no. 3-4, pp. 125–133, 2011.

[27] G. Lavecchia, P. Boncio, F. Brozzetti et al., "The April 2009 L'Aquila (central Italy) seismic sequence (M_w 6.3): a preliminary seismotectonic picture," *Recent Progress on Earthquake Geology*, p. 978, 2011.

[28] J. M. Fletcher, O. J. Teran, T. K. Rockwell et al., "Assembly of a large earthquake from a complex fault system: surface rupture kinematics of the 4 April 2010 El Mayor–Cucapah (Mexico) Mw 7.2 earthquake," *Geosphere*, vol. 10, no. 4, pp. 797–827, 2014.

[29] E. Aguirre, C. Benavente, L. Audin et al., "Earthquake surface ruptures on the altiplano and geomorphological evidence of normal faulting in the December 2016 (M_w 6.1) Parina earthquake, Peru," *Journal of South American Earth Sciences*, vol. 106, article 103098, 2021.

[30] F. Brozzetti, P. Boncio, D. Cirillo et al., "High-resolution field mapping and analysis of the August-October 2016 coseismic surface faulting (central Italy earthquakes): slip distribution, parameterization, and comparison with global earthquakes," *Tectonics*, vol. 38, no. 2, pp. 417–439, 2019.

[31] F. H. Swan, D. P. Schwartz, and L. S. Cluff, "Recurrence of moderate to large magnitude earthquakes produced by surface faulting on the Wasatch fault zone, Utah," *Bulletin of the Seismological Society of America*, vol. 70, pp. 1431–1462, 1980.

[32] D. P. Schwartz and K. J. Coppersmith, "Fault behavior and characteristic earthquakes: examples from the Wasatch and San Andreas fault zones," *Journal of Geophysical Research*, vol. 89, no. B7, pp. 5681–5698, 1984.

[33] M. N. Machette, S. F. Personius, and A. R. Nelson, "The Wasatch fault zone, USA," *Annales Tectonicae*, vol. 6, pp. 5–39, 1992.

[34] P. Zhang, D. B. Slemmons, and F. Mao, "Geometric pattern, rupture termination and fault segmentation of the Dixie Valley-Pleasant Valley active normal fault system, Nevada, U.S.A.," *Journal of Structural Geology*, vol. 13, no. 2, pp. 165–176, 1991.

[35] C. B. DuRoss, S. F. Personius, A. J. Crone et al., "Fault segmentation: new concepts from the Wasatch fault zone, Utah, USA," *Journal of Geophysical Research*, vol. 121, no. 2, pp. 1131–1157, 2016.

[36] G. Lavecchia, R. de Nardis, F. Ferrarini, D. Cirillo, S. Bello, and F. Brozzetti, "Regional seismotectonic zonation of hydrocarbon fields in active thrust belts: a case study from Italy," in *Building Knowledge for Geohazard Assessment and Management in the Caucasus and Other Orogenic Regions*, F. L. Bonali, F. Pasquaré Mariotto, and N. Tsereteli, Eds., Springer, the Netherlands, 2021.

[37] A. Pizzi and F. Galadini, "Pre-existing cross-structures and active fault segmentation in the northern- central Apennines (Italy)," *Tectonophysics*, vol. 476, no. 1-2, pp. 304–319, 2009.

[38] F. Ferrarini, P. Boncio, R. de Nardis et al., "Segmentation pattern and structural complexities in seismogenic extensional settings: the north Matese fault system (Central Italy)," *Journal of Structural Geology*, vol. 95, pp. 93–112, 2017.

[39] F. Iezzi, G. Roberts, J. F. Walker, and I. Papanikolaou, "Occurrence of partial and total coseismic ruptures of segmented normal fault systems: insights from the Central Apennines, Italy," *Journal of Structural Geology*, vol. 126, pp. 83–99, 2019.

[40] J. Faure Walker, P. Boncio, B. Pace et al., "Fault2SHA Central Apennines database and structuring active fault data for seismic hazard assessment," *Scientific Data*, vol. 8, no. 87, 2021.

[41] D. Cirillo, C. Totaro, G. Lavecchia et al., "Structural complexities and tectonic barriers controlling the recent seismic activity of the Pollino area (Calabria-Lucania, Southern Italy) – constraints from stress inversion and 3D fault model building," *Solid Earth*, vol. 13, pp. 205–228, 2022.

[42] C. Mansfield and J. Cartwright, "Fault growth by linkage: observations and implications from analogue models," *Journal of Structural Geology*, vol. 23, no. 5, pp. 745–763, 2001.

[43] C. von Hagke, M. Kettermann, N. Bitsch, D. Bücken, C. Weismüller, and J. L. Urai, "The effect of obliquity of slip in normal faults on distribution of open fractures," *Frontiers in Earth Science*, vol. 7, p. 18, 2019.

[44] R. L. Bruhn, P. R. Gibler, and W. T. Parry, "Rupture characteristics of normal faults: an example from the Wasatch fault zone, Utah," in *Continental Extensional Tectonics*, M. P. Coward, J. F. Dewey, and P. L. Hancock, Eds., vol. 28, pp. 337–353, Geological Society of London Special Publication, 1987.

[45] A. J. Crone and K. M. Haller, "Segmentation and the coseismic behavior of basin and range normal faults: examples from east-central Idaho and southwestern Montana, U.S.A.," *Journal of Structural Geology*, vol. 13, no. 2, pp. 151–164, 1991.

[46] S. U. Janecke, "Structures in segment boundary zones of the Lost River and Lemhi faults, east central Idaho," *Journal of Geophysical Research Solid Earth*, vol. 98, no. B9, pp. 16223–16238, 1993.

[47] W. E. Scott, K. L. Pierce, and M. H. Hait, "Quaternary tectonic setting of the 1983 Borah Peak earthquake, central Idaho," *Bulletin of the Seismological Society of America*, vol. 75, pp. 1053–1066, 1985.

[48] D. D. Susong, S. U. Janecke, and R. L. Bruhn, "Structure of a fault segment boundary in the Lost River fault zone, Idaho, and possible effect on the 1983 Borah Peak earthquake rupture," *Bulletin of the Seismological Society of America*, vol. 80, no. 1, pp. 57–68, 1990.

[49] M. P. Bunds, C. B. DuRoss, R. D. Gold et al., *High resolution topography of the northern 16 km of the M6.9 1983 Borah Peak earthquake surface rupture on the Lost River fault zone, Idaho, USA*, OpenTopography, 2019.

[50] M. P. Bunds, C. B. DuRoss, R. D. Gold et al., *Lost River fault at Doublespring Pass Rd, Idaho 2015*, Utah Valley University (UVU), 2020, Distributed by OpenTopography.

[51] D. A. Storchak, D. Di Giacomo, I. Bondar et al., "Public release of the ISC-GEM global instrumental earthquake catalogue (1900-2009)," *Seismological Research Letters*, vol. 84, no. 5, pp. 810–815, 2013.

[52] D. A. Storchak, D. Di Giacomo, E. R. Engdahl et al., "The ISC-GEM global instrumental earthquake catalogue (1900-2009): introduction," *Physics of the Earth and Planetary Interiors*, vol. 239, pp. 48–63, 2015.

[53] D. Di Giacomo, E. R. Engdahl, and D. A. Storchak, "The ISC-GEM earthquake catalogue (1904-2014): status after the extension project," *Earth System Science Data*, vol. 10, no. 4, pp. 1877–1899, 2018.

[54] US Geological Survey and Idaho Geological Survey, "Quaternary fault and fold database for the United States," 2020, https://www.usgs.gov/natural-hazards/earthquake-hazards/faults.

[55] S. Bello, C. Scott, R. Arrowsmith, and T. Scott, *High resolution topography along the Lost River Valley, Idaho 2019*, OpenTopography, 2020.

[56] M. J. Westoby, J. Brasington, N. F. Glasser, M. J. Hambrey, and J. M. Reynolds, "'Structure-from-Motion' photogrammetry: A low-cost, effective tool for geoscience applications," *Geomorphology*, vol. 179, pp. 300–314, 2012.

[57] K. Johnson, E. Nissen, S. Saripalli et al., "Rapid mapping of ultrafine fault zone topography with structure from motion," *Geosphere*, vol. 10, no. 5, pp. 969–986, 2014.

[58] A. Salach, K. Bakula, M. Pilarska, W. Ostrowski, K. Górski, and Z. Kurczynski, "Accuracy assessment of point clouds from LiDAR and dense image matching acquired using the UAV platform for DTM creation," *ISPRS International Journal of Geo-Information*, vol. 7, no. 9, p. 342, 2018.

[59] D. Cirillo, "Digital field mapping and drone-aided survey for structural geological data collection and seismic hazard assessment: case of the 2016 central Italy earthquakes," *Applied Sciences*, vol. 10, no. 15, p. 5233, 2020.

[60] C. J. Crosby, J. R. Arrowsmith, and V. Nandigam, "Zero to a trillion: Advancing Earth surface process studies with open access to high-resolution topography," *Developments in Earth Surface Processes*, vol. 23, pp. 317–338, 2020.

[61] D. C. P. Peacock and D. J. Sanderson, "Geometry and development of relay ramps in normal fault systems," *AAPG Bulletin*, vol. 78, no. 2, pp. 147–165, 1994.

[62] R. S. Yeats, K. Sieh, and C. R. Allen, *The Geology of Earthquakes*, Oxford University Press, 1997.

[63] J. G. Ramsay and R. Lisle, "The techniques of modern structural geology," *Applications of Continuum Mechanics in Structural Geology*, vol. 3, pp. 702–1061, 2000.

[64] H. Fossen, *Structural Geology*, Cambridge University Press, 2010.

[65] J. McCalpin, *Paleoseismology*, California, Academic Press, San Diego, 2nd edition, 2009.

[66] G. H. Davis, S. J. Reynolds, and C. F. Kluth, *Structural Geology of Rocks and Regions*, John Wiley & Sons, Inc., 3rd edition, 2011.

[67] S. S. Xu, L. G. Velasquillo-Martinez, J. M. Grajales-Nishimura, G. Murillo-Munetòn, and A. F. Nieto-Samaniego, "Methods for quantitatively determining fault slip using fault separation," *Journal of Structural Geology*, vol. 29, no. 10, pp. 1709–1720, 2007.

[68] R. W. Allmendinger, N. Cardozo, and D. Fisher, *Structural Geology Algorithms*, Cambridge University Press, New York, 2012.

[69] J. Angelier and P. Mechler, "Sur une me'thode graphique de recherche des contraintes principales egalement utilisable en tectonique et en seismologie: la methode des diedres droits," *Bulletin de la Société géologique de France*, vol. 7, pp. 1309–1318, 1977.

[70] P. Boncio, F. Liberi, M. Caldarella, and F. C. Nurminen, "Width of surface rupture zone for thrust earthquakes: implications for earthquake fault zoning," *Natural Hazards and Earth System Sciences*, vol. 18, no. 1, pp. 241–256, 2018.

[71] P. Boncio, P. Galli, G. Naso, and A. Pizzi, "Zoning surface rupture hazard along normal faults: insight from the 2009 M_w 6.3 L'Aquila, Central Italy, earthquake and other global earthquakes," *Bulletin of the Seismological Society of America*, vol. 102, no. 3, pp. 918–935, 2012.

[72] I. Manighetti, M. Campillo, C. Sammis, P. M. Mai, and G. King, "Evidence for self-similar, triangular slip distributions on earthquakes: implications for earthquake and fault mechanics," *Journal of Geophysical Research: Solid Earth*, vol. 110, no. B5, article B05302, 2005.

[73] O. Zielke, Y. Klinger, and J. R. Arrowsmith, "Fault slip and earthquake recurrence along strike-slip faults – Contributions of high-resolution geomorphic data," *Tectonophysics*, vol. 638, pp. 43–62, 2015.

[74] W. Thatcher, "Present-day crustal movements and the mechanics of cyclic deformation," in *The San Andreas Fault system, California*, R. E. Wallace, Ed., pp. 189–205, U.S. Geological Survey Professional Paper, 1515, 1990.

[75] P. Somerville, K. Irikura, R. Graves et al., "Characterizing crustal earthquake slip models for the prediction of strong ground motion," *Seismological Research Letters*, vol. 70, no. 1, pp. 59–80, 1999.

[76] I. Manighetti, M. Campillo, S. Bouley, and F. Cotton, "Earthquake scaling, fault segmentation, and structural maturity," *Earth and Planetary Science Letters*, vol. 253, no. 3–4, pp. 429–438, 2007.

[77] K. M. Haller and A. J. Crone, "Twenty years after the Borah Peak earthquake: field guide to surface-faulting earthquakes along the Lost River fault, Idaho," in *Geological Field Trips in Southern Idaho, Eastern Oregon, and Northern Nevada*, K. M. Haller and S. H. Wood, Eds., pp. 118–135, U.S. Geological Survey Open-File Report 2004-1222, 2004.

[78] S. G. Wesnousky, "Predicting the endpoints of earthquake ruptures," *Nature*, vol. 444, no. 7117, pp. 358–360, 2006.

[79] G. P. Biasi and S. G. Wesnousky, "Steps and gaps in ground ruptures: empirical bounds on rupture propagation," *Bulletin of the Seismological Society of America*, vol. 106, no. 3, pp. 1110–1124, 2016.

[80] G. P. Biasi and S. G. Wesnousky, "Bends and ends of surface ruptures," *Bulletin of the Seismological Society of America*, vol. 107, no. 6, pp. 2543–2560, 2017.

[81] M. Meghraoui, V. Bosi, and T. Camelbeeck, "Fault fragment control in the 1997 Umbria-Marche, central Italy, earthquake sequence," *Geophysical Research Letters*, vol. 26, no. 8, pp. 1069–1072, 1999.

[82] Y. Klinger, "Relation between continental strike-slip earthquake segmentation and thickness of the crust," *Journal of Geophysical Research*, vol. 115, no. B7, 2010.

[83] A. Christophersen, N. Litchfield, K. Berryman et al., "Development of the global earthquake model's neotectonic fault database," *Natural Hazards*, vol. 79, no. 1, pp. 111–135, 2015.

[84] J. P. Faure Walker, G. P. Roberts, P. A. Cowie et al., "Horizontal strain-rates and throw-rates across breached relay zones, central Italy: implications for the preservation of throw deficits at points of normal fault linkage," *Journal of Structural Geology*, vol. 31, no. 10, pp. 1145–1160, 2009.

[85] F. Iezzi, Z. Mildon, J. F. Walker et al., "Coseismic throw variation across along-strike bends on active normal faults: implications for displacement versus length scaling of earthquake ruptures," *Journal of Geophysical Research: Solid Earth*, vol. 123, no. 11, pp. 9817–9841, 2018.

[86] F. Iezzi, G. P. Roberts, and J. Faure Walker, "Throw-rate variations within linkage zones during the growth of normal faults: case studies from the western Volcanic Zone, Iceland," *Journal of Structural Geology*, vol. 133, article 103976, 2020.

[87] D. Wu and L. Bruhn, "Geometry and kinematics of active normal faults, South Oquirrh Mountains, Utah: implication for fault growth," *Journal of Structural Geology*, vol. 16, no. 8, pp. 1061–1075, 1994.

[88] M. F. Ferrario and F. Livio, "Characterizing the distributed faulting during the 30 October 2016, Central Italy earthquake: a reference for fault displacement hazard assessment," *Tectonics*, vol. 37, no. 5, pp. 1256–1273, 2018.

[89] O. J. Teran, J. M. Fletcher, M. E. Oskin et al., "Geologic and structural controls on rupture zone fabric: a field-based study of the 2010 Mw 7.2 El Mayor–Cucapah earthquake surface rupture," *Geosphere*, vol. 11, no. 3, pp. 899–920, 2015.

[90] M. E. Oskin, J. R. Arrowsmith, A. H. Corona et al., "Near-field deformation from the El Mayor-Cucapah earthquake revealed by differential LIDAR," *Science*, vol. 335, no. 6069, pp. 702–705, 2012.

[91] G. Schmalzle, T. Dixon, R. Malservisi, and R. Govers, "Strain accumulation across the Carrizo segment of the San Andreas fault, California: impact of laterally varying crustal properties," *Journal of Geophysical Research*, vol. 111, no. B5, article B05403, 2006.

[92] R. Zinke, J. Hollingsworth, and J. F. Dolan, "Surface slip and off-fault deformation patterns in the 2013 M_W 7.7 Balochistan, Pakistan earthquake: implications for controls on the distribution of near-surface coseismic slip," *Geochemistry, Geophysics, Geosystems*, vol. 15, no. 12, pp. 5034–5050, 2014.

[93] C. P. Scott, J. R. Arrowsmith, E. Nissen, L. Lajoie, T. Maruyama, and T. Chiba, "TheM7 2016 Kumamoto, Japan, earthquake: 3-D deformation along the fault and within the damage zone constrained from differential lidar topography," *Journal of Geophysical Research: Solid Earth*, vol. 123, no. 7, pp. 6138–6155, 2018.

[94] C. Scott, M. Bunds, M. Shirzaei, and N. Toke, "Creep along the Central San Andreas Fault from surface fractures, topographic differencing, and InSAR," *Journal of Geophysical Research: Solid Earth*, vol. 125, no. 10, 2020.

[95] C. P. Scott, S. B. DeLong, and J. R. Arrowsmith, "Distribution of aseismic deformation along the Central San Andreas and Calaveras faults from differencing repeat airborne lidar," *Geophysical Research Letters*, vol. 47, no. 22, article e2020GL090628, 2020.

[96] M. F. Ferrario and F. Livio, "Distributed faulting following normal earthquakes: reassessment and updating of scaling relations," *Solid Earth*, vol. 1, 2020.